USGS
science for a changing world

**Prepared for the National Aeronautics and Space Administration**

# Geologic Map of the Agnesi Quadrangle (V–45), Venus

By Vicki L. Hansen and Erik R. Tharalson

Pamphlet to accompany
Scientific Investigations Map 3250

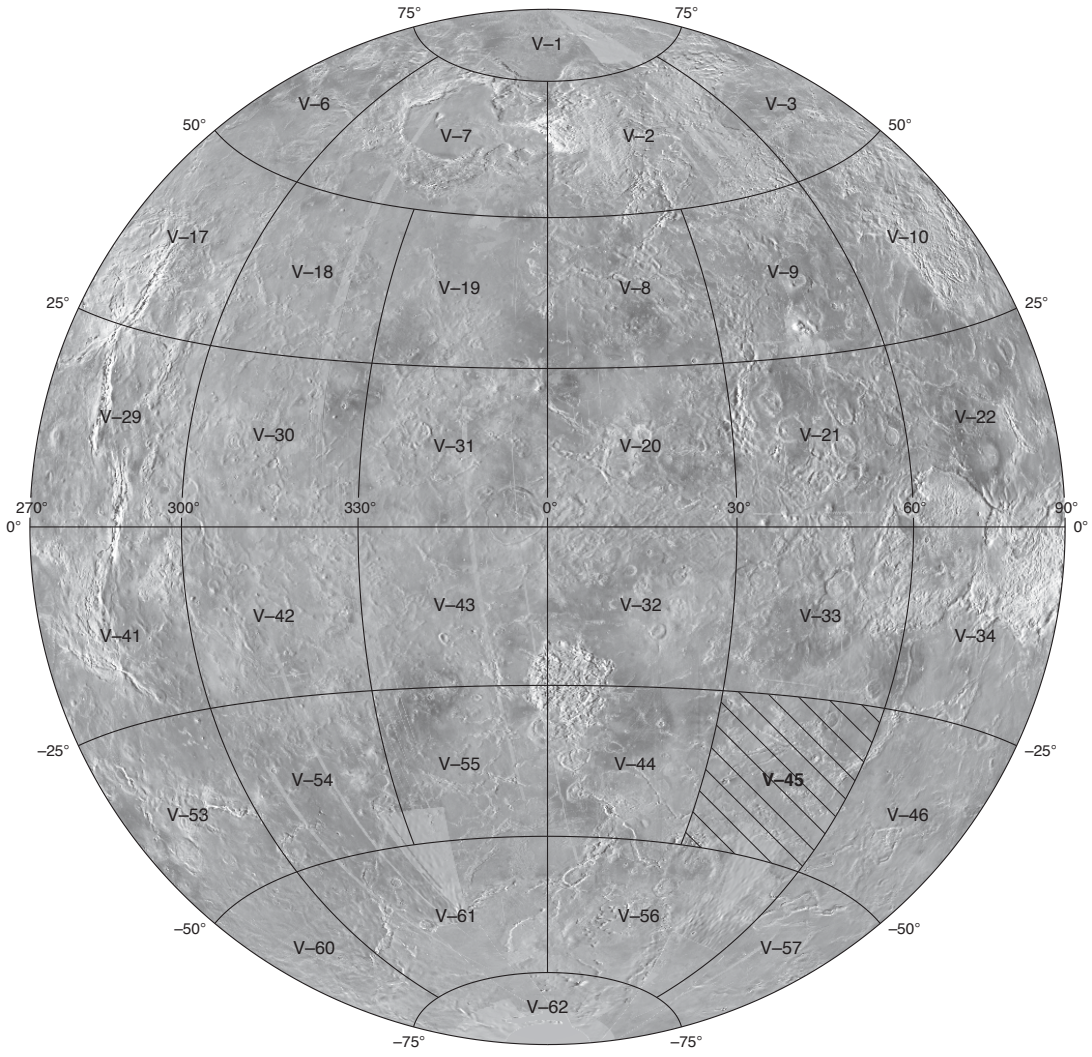


2014

**U.S. Department of the Interior**
**U.S. Geological Survey**

# Contents



# Tables

# Geologic Map of the Agnesi Quadrangle (V–45), Venus

By Vicki L. Hansen and Erik R. Tharalson

## The Magellan Mission

The Magellan spacecraft orbited Venus from August 10, 1990, until it plunged into the Venusian atmosphere on October 12, 1994. Magellan Mission objectives included (1) improving the knowledge of the geological processes, surface properties, and geologic history of Venus by analysis of surface radar characteristics, topography, and morphology and (2) improving the knowledge of the geophysics of Venus by analysis of Venusian gravity.

The Magellan spacecraft carried a 12.6-cm-wavelength (S-band) radar system to map the surface of Venus. The transmitter and receiver systems were used to collect three datasets: (1) synthetic aperture radar (SAR) images of the surface, (2) passive microwave thermal emission observations, and (3) measurements of the backscattered power at small angles of incidence, which were processed to yield altimetric data. Radar imaging and altimetric and radiometric mapping of the Venusian surface were accomplished in mission cycles 1, 2, and 3 from September 1990 until September 1992. Ninety-eight percent of the surface was mapped with radar resolution on the order of 120 m. The SAR observations were projected to a 75-m nominal horizontal resolution, and these full-resolution data compose the image base used in geologic mapping. The primary polarization mode was horizontal-transmit, horizontal-receive (HH), but additional data for selected areas were collected for the vertical polarization sense. Incidence angles varied between about 20° and 45°.

High-resolution Doppler tracking of the spacecraft took place from September 1992 through October 1994 (mission cycles 4, 5, and 6). Approximately 950 orbits of high-resolution gravity observations were obtained between September 1992 and May 1993 while Magellan was in an elliptical orbit with a periapsis near 175 km and an apoapsis near 8,000 km. An additional 1,500 orbits were obtained following orbit-circularization in mid-1993. These data exist as a 75° by 75° harmonic field.

### Magellan Radar Data

Radar backscatter power is determined by (1) the morphology of the surface at a broad range of scales and (2) the intrinsic reflectivity, or dielectric constant, of the material. Topography at scales of several meters and larger can produce quasi-specular echoes, and the strength of the return is greatest when the local surface is perpendicular to the incident beam. This type of scattering is most important at very small angles of incidence, because natural surfaces generally have few large tilted facets at high angles. The exception is in areas of steep slopes, such as ridges or rift zones, where favorably tilted terrain can produce very bright signatures in the radar image. For most other areas, diffuse echoes from roughness at scales comparable to the radar wavelength are responsible for variations in the SAR return. In either case, the echo strength is also modulated by the reflectivity of the surface material. The density of the upper few wavelengths of the surface can have a significant effect. Low-density layers, such as crater ejecta or volcanic ash, can absorb the incident energy and produce a lower observed echo. On Venus, a rapid increase in reflectivity exists at a certain critical elevation above which high-dielectric minerals or coatings are thought to be present. This leads to bright SAR echoes from virtually all areas above that critical elevation.

The measurements of passive thermal emission from Venus, though of much lower spatial resolution than the SAR data, are more sensitive to changes in the dielectric constant of the surface than to roughness. They can be used to augment studies of the surface and to discriminate between roughness and reflectivity effects. Observations of the near-nadir backscatter power, collected using a separate smaller antenna on the spacecraft, were modeled using the Hagfors expression for echoes from gently undulating surfaces to yield estimates of planetary radius, Fresnel reflectivity, and root-mean-square (RMS) slope. The topographic data produced by this technique have horizontal footprint sizes of about 10 km near periapsis and a vertical resolution on the order of 100 m. The Fresnel reflectivity data provide a comparison to the emissivity maps, and the RMS slope parameter is an indicator of the surface tilts, which contribute to the quasi-specular scattering component.

## Agnesi Quadrangle

### Introduction

The Agnesi quadrangle (V–45), named for centrally located Agnesi crater, encompasses approximately 6,500,000 km$^2$ extending from lat 25° to 50° S. and from long 30° to 60° E. The V–45 quadrangle lies within Venus' lowland broadly between highlands Ovda Regio to the northeast and Alpha Regio to the west. The region ranges in altitude from 6,051 to 6,054 km, with an average of ~6,052 km, which is essentially mean planetary radius. The quadrangle displays a wide range of features including large to small arcuate exposures of

ribbon-tessera terrain (Hansen and Willis, 1998), ten lowland coronae, two montes, 13 pristine impact craters, and long but localized volcanic flows sourced to the west in V–44. Shield terrain (Hansen 2005) occurs across much of the V–45 quadrangle. Although V–45 lies topographically within the lowland, it includes only one planitia (Fonueha Planitia), perhaps because the features mentioned decorate it.

Geologic mapping of the Agnesi quadrangle (V–45) provides an opportunity (1) to examine the nature of lowland ribbon-tessera terrain, as compared to highland ribbon-tessera terrain; (2) to examine the nature and history of lowland coronae and montes to evaluate hypotheses for the evolution of these features; and (3) to evaluate global catastrophic/episodic resurfacing hypotheses.

Ribbon-tessera terrain (Hansen and Willis, 1998), a structurally distinctive terrain marked by roughly orthogonal fold axes and ribbon troughs, characterizes Venusian crustal plateaus (Hansen and others, 1999), although this distinctive fabric is also variably preserved across some lowland regions (Hansen and Willis, 1996, 1998), including the Agnesi quadrangle. Isolated kipukas of ribbon-tessera terrain protrude through the shield-terrain veneer and preserve evidence of local surface processes that predated shield-terrain emplacement, including those leading to regional development of tessera terrain fabrics. The ribbon-tessera fabrics are similar to the fabrics that characterize high-standing crustal plateaus, such as nearby Ovda and Alpha Regiones. Ribbon-bearing kipukas may preserve evidence of ancient collapsed crustal plateaus (Phillips and Hansen, 1994; Ivanov and Head, 1996; Hansen and Willis, 1998; Ghent and Tibuleac, 2002), or they may record different, but rheologically similar, processes.

Geologic mapping of the V–45 quadrangle constrains the geologic history of 12 lowland coronae and montes. Lowland coronae are relatively rare (10% of coronae); they do not form chains, typical of mesoland coronae (Phillips and Hansen, 1994), nor do they cluster, typical of highland coronae associated with volcanic rises (Stofan and others, 2001). The evolution of all coronae, whether by a single mechanism or a range of mechanisms, is a topic of debate (for example, Stofan and others, 1992, 2001; Vita-Finzi and others, 2005; Hamilton, 2005). The V–45 quadrangle hosts about 20 percent of the lowland coronae on Venus; the geologic history of these features should provide critical insight toward understanding coronae evolution.

Two general classes of hypotheses have emerged to address the near random spatial distribution of ~970 apparently pristine impact craters across the surface of Venus: (1) catastrophic/episodic resurfacing and (2) equilibrium/evolutionary resurfacing. Catastrophic/episodic hypotheses propose that a global-scale, temporally punctuated event or events dominated Venus' evolution and that the generally uniform impact crater distribution (Schaber and others, 1992; Phillips and others, 1992; Herrick and others, 1997) reflects craters that accumulated during relative global quiescence since that event (for example, Strom and others, 1994; Herrick, 1994; Turcotte and others, 1999). Equilibrium/evolutionary hypotheses suggest instead that the near random crater distribution results from relatively continuous, but spatially localized, resurfacing in which volcanic and (or) tectonic processes occur across the planet through time, although the style of operative processes may have varied temporally and spatially (for example, Phillips and others, 1992; Guest and Stofan, 1999; Hansen and Young, 2007). Geologic relations within the map area allow us to test the catastrophic/episodic versus equilibrium/evolutionary resurfacing hypotheses.

## Data

Data used for the construction of the geologic map include correlated digital NASA Magellan datasets: full resolution (~100 m/pixel) synthetic aperture radar (SAR) images, altimetry, synthetic stereo images, RMS slope data, and emissivity data. The geomorphic features within V–45 lie below the resolution of available gravity data owing to their relatively small sizes.

### Image Data

Data for this study were provided by the U.S. Geological Survey (USGS) Astrogeology Team in the projection parameters for the Agnesi (V–45) quadrangle (Lambert conformal conic, standard parallels at 34° S. and 73° S., central meridian 45° E., latitude of origin 90° S.). The data are available online from the USGS Map-a-planet website (http://pdsmaps.wr.usgs.gov/) and the USGS Planetary GIS Web Server (http://webgis.wr.usgs.gov/) in a variety of formats, although not necessarily in the projection parameters used herein. Cycle 1 (east-directed illumination, or left-looking) SAR images cover the V–45 map area, except for the southeast corner from 45–50° S. and ~41–60° E. Cycle 2 (west-directed illumination, or right-looking) SAR data forms a 7°-wide swath along the eastern edge of the quadrangle. Cycle 3 left-look stereo SAR coverage across the V–45 map area is rare, and it consists of a thin, <1°-wide sliver along the northeastern edge of the quadrangle (Ford and others, 1993). Digital Compressed Once Mosaicked Image Data Records (C1-MIDR; 225 m/pixel) SAR data from the regional database and map base and digital full-resolution radar map (FMAP; 75–125 m/pixel) dataset were used in constructing the geologic map. Ancillary data included the Global Topographic Data Record 3 (GTDR 3) that has an effective horizontal resolution of 10 km and similar products representing Fresnel reflectivity at 12.6-cm wavelength, average 1- to 10-m-scale slope, and derived 12.6-cm emissivity data (GRDR, GSDR, and GEDR, respectively). GTDR data were combined with SAR images to produce synthetic stereo anaglyphs (Kirk and others, 1992) using NIH-Image macros developed by D.A. Young. These images played a critical role in elucidating the relations between geology and topography and, in particular, the interaction of flows, primary and secondary structures, and topography.

### Image Interpretation

The interpretation of features in Magellan SAR images is key to developing a geologic history for the Agnesi quadrangle. Ford and others (1993) explored the subject of radar image interpretation in depth.

The methodology for defining geologic units and structural fabrics builds on standard geologic analysis detailed by Wilhelms (1990) and Tanaka (1994), but we also considered the cautions of Hansen (2000), Zimbelman (2001), Skinner and Tanaka (2003), and McGill and Campbell (2004). Map units represent material emplaced within an increment of geologic history, to which standard stratigraphic methods have some limited application; however, some units may be composite, because they might not be stratigraphically coherent over their entire represented area and (or) they may have been emplaced over an extended period of time, particularly in relation to other units and (or) formation of secondary structures. Attempts were made to clearly separate secondary structures from material units; locations, orientations, and relative densities of primary and secondary structures are shown independent of material units on the map. Evidence for reactivation of secondary structures is common across the map area, which further complicates the process of unraveling both temporal constraints and history.

Criteria for distinguishing discrete geologic units in the map area include (1) the presence of sharp, continuous contacts; (2) truncation of, or interaction with, underlying secondary structures and topography; and (3) primary structures, for example flow channels or edifice topography, that allow a reasonable geologic interpretation and hint at three-dimensional geometry. Some mapped units do not fit these constraints, which limits their use in constructing stratigraphic interpretations. Composite units, in particular, cannot provide reasonable temporal constraints, even of a relative nature.

Estimating absolute geologic age is not currently possible for the surface of Venus. Unlike surface crater statistics for planetary bodies that have old surfaces and high crater densities, such as the Moon and Mars, Venus impact crater statistics cannot place constraints on the age of surface units that cover the small areas visible in the map area (Hauck and others, 1998; Campbell, 1999). Relative age constraints may be established only where units are in mutual contact and (or) interact with the same suite of secondary structures. Such relative temporal constraints are only locally applicable and cannot be extended across the map area with confidence, nor are they valid for composite (time-transgressive) geologic units.

Ranges of structures, both primary (depositional or emplacement-related) and secondary (tectonic), are identified in the Magellan SAR data. Primary structures include channels, shields, lobate flow fronts, and impact crater haloes and rims. Channels are sinuous, low-backscatter troughs hundreds of kilometers long and a few kilometers wide; locally, they may lack apparent topographic relief (Baker and others, 1992, 1997). Shields are small (generally 1 to 15 km in diameter, rarely 20 km in diameter), quasi-circular to circular, radar-dark or radar-bright features with or without topographic expression and with or without a central pit (Guest and others, 1992). The size of individual shields is difficult to constrain because bases of individual shields are typically poorly defined, and deposits commonly blend smoothly into a composite layer that cannot be treated as a time line or marker unit with any certainty. Pits, sharply defined depressions, or pit chains, linear arrays of pits, likely represent regions marked by subsurface excavation and, as such, they may mark the surface expression of dilatational faults or dikes (Grosfils and Head, 1994; Okubo and Martel, 1998; Bleamaster and Hansen, 2005; Ferrill and others, 2004; Schultz and others, 2004). Pits or pit chains can be considered primary structures or secondary structures, depending on the question at hand; pits are primary structures relative to pit-related materials, yet they may be secondary structures relative to the units they cut or are emplaced within.

Most radar lineaments represent secondary structures. Stofan and others (1993) provided an excellent introduction to the interpretation of secondary structures in Magellan SAR imagery. Extremely fine, sharply defined, continuous radar-bright lineaments, typically present in the lowlands, have commonly been interpreted as fractures (Banerdt and Sammis, 1992; Banerdt and others, 1997). If a fracture is associated with pits, it may represent the surface expression of a subsurface dike or a dilatational fault. Paired parallel dark and light lineaments, separated by more than a few kilometers, that define linear troughs are generally interpreted as grabens.

In SAR imagery, the opposite of a groove (linear trough) is a ridge (positive linear topography marked by parallel light and dark lineaments with the light lineament closest to illumination direction). On Venus, ridges typically have either parallel edges with moderate sinuosity at the 10-km scale and an across-strike gradation in backscatter (a form specifically called ridges herein), or they have a more erratic plan view, with common high-angle interruptions at the 10-km scale and variations in across-strike width (wrinkle ridges). Warps consist of positive linear topographic features, approximately 100 km across and thousands of kilometers long; warps, which are too subtle to appear prominently in SAR data, are discernable in topographic data.

Parallel bright and dark lineaments that form a fabric marked by alternating parallel ridges and troughs with typical wavelengths of 2 to 5 km are called ribbons, ribbon fabric, or ribbon terrain (Hansen and Willis, 1996, 1998). Bindschadler and others (1992) called ribbons "narrow troughs." Ribbon fabrics are commonly spatially associated with folds, and the fold crests typically trend at a high angle (generally 90°) to the ribbon lineaments. Together, ribbons and folds characterize ribbon-tessera terrain (Hansen and Willis, 1996, 1998). Graben complexes, also commonly spatially associated with ribbons, typically parallel ribbon trends, but graben complexes can be differentiated from ribbons on the basis of smaller length-to-width ratios. Graben complexes that occur within ribbon terrain typically cut across fold crests, which results in a lens-shape plan view. Collectively referred to as ribbon-tessera terrain, or ribbon terrain for short, this distinctive composite tectonic fabric commonly marks tessera terrain. The composite fabric may reflect a progressive increase in the depth to the rheological brittle-ductile transition with time and fabric development (Hansen and Willis, 1998; Ghent and Hansen, 1999; Brown and Grimm, 1999). For a discussion of ribbon-terrain controversies, see Gilmore and others (1998) and Hansen and others (2000).

## Geologic Setting

The V–45 quadrangle is nestled between two highland crustal plateaus, Ovda Regio to the northeast and Alpha Regio to the west, and lowland regions of Tinatin Planitia to the northwest and Aino Planitia to the southwest. Lada Terra lies to the south. We use the term "lowland" to describe broad, regional, long-wavelength (more than hundreds of kilometers across) topographic basins, and "planitia/planitiae" in reference to individual geomorphic basins or lowland regions. We use the term "plains" only to describe geologic units, and only when the referenced published work uses that term. Technically V–45 lies within the lowlands of Venus, although this particular lowland region includes a wide variety of topographic, geomorphic, structural, and geologic features.

## Geologic Relations

The Agnesi quadrangle lies within the southern hemisphere lowlands, with an average elevation of ~6,052 km similar to mean planetary radius; however, it includes local elevations as much as 6,053.5 km, and Xcanil Corona marks the lowest elevation at 6,050.8 km (fig. 1*A*). Although the V–45 quadrangle shows a relatively narrow range of elevations, it shows a wide range of RMS slope values and radar backscatter values (figs. 1*B–D*); each dataset reflects the wide variation in types of features preserved within the map area.

Regionally, V–45 lies lower in the east than the west and lower in the south than the north (although altimetry data is lacking across much of southernmost V–45). Eastern V–45 slopes gently eastward, whereas the south-central and southeastern parts of V–45 are characterized by short-wavelength topography. The V–45 quadrangle includes linear to curvilinear ridges, local highs that host Pasom-mana, Xi Wang-mu, and Tushita Tesserae and several domical coronae in the northwest and southeast parts of the map area.

RMS slope values range from 0 to 5 across V–45. Ridges display linear high RMS slope values, whereas the tesserae correlate with a wormy pattern marked by subdued variations in RMS slope values, and the coronae typically show circular RMS slope patterns marked by high to intermediate values, with some coronae showing double RMS slope rings (fig. 1*B*). Finueha Planitia and northeastern V–45 show the lowest and most regionally consistent RMS slope values within the quadrangle.

Finueha Planitia and the northeastern part of V–45 also represent the lowest regionally extensive regions within V–45. The linear to curvilinear ridges and regionally extensive highs within V–45 host Pasom-mana, Xi Wang-mu, and Tushita Tesserae in the north-central, east, and southeast-central areas, respectively. Domical coronae (Inanna, Elihino, Codidon, and Mou-nyamy Coronae) and basinal coronae (Mama-Allpa, Umay-ene, Zemlika, and Xcanil Coronae) are equally distributed across the map area, showing no particular geometric pattern. Fonueha Planitia, which trends east to the south of west-northwest-trending Tushita Tesserae, is narrow and relatively poorly defined compared to other Venusian planitiae.

The V–45 quadrangle shows about equal areas of radar rough versus radar smooth regions, representing a wide variation in features (figs. 1*C–D*). Tessera terrains correlate with high-backscatter values, whereas topographic low regions generally correlate with low-radar backscatter. In the northwestern part of the quadrangle, three nested curvilinear ridges define concentric circles with diameters of 900 to 1,200 km. The three ridges, each 75 to 100 km wide and hundreds of kilometers long, are separated by 100- to 200-km-wide ridge-parallel basins. The central ridge includes Artio Chasma, a linear trough flanked by narrow parallel ridges. The northern and central ridges (including Artio Chasma) host linear tracts of ribbon-tessera terrain; the southern ridge hosts buried ribbon-tessera terrain. The tessera fold fabric parallels the ridge crests and intervening elongate basins. The V–45 quadrangle also hosts 10 lowland coronae, 2 montes, and 13 pristine impact craters, each of which stand out in SAR data. Sezibwa Vallis, in the southwestern part of the map area, hosts long flows as much as hundreds of kilometers in length, sourced from V–44 to the west. Shield terrain, best observed in full-resolution SAR data, occurs across much of V–45. Also best observed in high-resolution SAR images, regional fractures trend east-northeast across much of V–45. The northeast corner of V–45 preserves the only tract of wrinkle ridges, which trend north-northwest, perpendicular to east-northeast-trending fractures. Gaps in Magellan altimetry and SAR data for south-central V–45 disallow geologic mapping in that part of the quadrangle.

Geologic map units are broadly divisible into six packages: (1) ribbon-tessera terrains and associated units; (2) shield terrain; (3) lowland basin flows, including smooth flows and undivided flows; (4) V–45 corona-related flows or deposits; (5) flows sourced from regions to the west (V–44, Kalwin quadrangle) and the east (V–46, Aino quadrangle); and (6) impact crater-related deposits.

### Terrain Units

The term "terrain" describes a texturally defined region, for example, a region where tectonism imparted a surface with a penetrative deformation that disallows interpretation of the original unit or units (Wilhelms, 1990). Characteristic texture could imply a shared history, such as a terrestrial tectonothermal history or an event that melds possibly previously unrelated rock units (any combination of igneous, metamorphic, and sedimentary rocks) into gneissic terrain; no unique history is inferred or required prior to the event(s) that melded potentially separate units into the textural terrain. Events prior to terrain formation are unconstrained in time or process unless specifically noted. Two general classes of basal units occur across V–45: ribbon-tessera terrain and associated units and shield terrain.

#### Ribbon-tessera Terrain and Related Units

Three different ribbon-tessera fabrics are preserved within V–45: orthogonal ribbon-fold tessera, S-C tessera, and southern V–45 tessera (figs. 2 and 3). Orthogonal ribbon-fold tessera displays near orthogonal ribbon troughs and fold axes (fig. 2).

Fold wavelengths range from tens of kilometers to less than one kilometer, essentially to the effective resolution (Zimbelman, 2001) of the Magellan SAR data for folds. Ribbon wavelengths range from 5 to 2 km, and below, again to the effective resolution of the Magellan SAR data. Orthogonal ribbon-fold fabrics are the most common tessera fabric across V–45 as they are for ribbon-tessera terrain globally (Hansen and Willis, 1996).

S-C ribbon-tessera fabrics (fig. 2) occur locally within long topographic ridges paralleled with linear valleys, such as along Artio Chasma. S-C tessera fabric, first described by Hansen (1992) and discussed at length by Hansen and Willis (1996), shows a fabric asymmetry comprised of ductile and brittle structures that together define coherent pictures of noncoaxial strain-reflecting relative shear displacement, similar to S-C fabrics within terrestrial ductile shear zones (for example, Berthé and others, 1979). S-C tessera fabrics record horizontal displacement across zones that are tens to hundreds of kilometers wide; interpreted shear directions are shown on the geologic map. Both orthogonal ribbon-fold fabric and the S-C tessera fabric characterize ribbon-tessera terrain preserved within crustal plateaus. S-C tessera fabric represents ductile shear zones in central Ovda Regio, along its southern margin and along its eastern margin with Thetis Regio (Ghail, 2002; Tuckwell and Ghail, 2003; Ignacio and others, 2005; Kumar, 2005; Romeo and others, 2005). Orthogonal ribbon-fold fabric and S-C tessera fabric could represent the deformation of the surface scum of huge crystallizing lava ponds (Hansen, 2006). Hawaii's lava lakes show dynamic flow fabrics of extension, convergence, and strike-slip translation similar to terrestrial plate tectonic kinematic patterns, presumably driven by convection within the lava lake. Similarly, Ovda's ancient lava pond surface could record layer-parallel shortening and orthogonal extension (forming orthogonal ribbon-fold tessera fabric), along with localized horizontal shear distributed over several hundreds of kilometers (forming S-C tessera fabric).

Ribbon-tessera terrain is divided into four units on the basis of regional continuity and the orientation of ribbon-fold structures: (1) unit rtP (Pasom-mana ribbon-tessera terrain) with facies a, b, and c delineated on the basis of possible crosscutting relations, (2) unit rtTX (Tushita and Xi Wang-mu ribbon-tessera terrain), (3) unit rtE (Ekhe-Burkhan ribbon-tessera terrain), and (4) unit rtu (ribbon-tessera terrain, undivided). The various ribbon-tessera terrain units are differentiated using regional location and structural trends. It is unclear how the various units are related to one another temporally because interpretations of crosscutting relations are not unique. We also define two units associated with ribbon-tessera terrain: intratessera basin material unit itb, delineated on the basis of ribbon-tessera terrain association, and undivided buried ribbon tessera, unit rtc.

Pasom-mana ribbon-tessera terrain includes facies $rtP_a$, $rtP_b$, and $rtP_c$. We identify these members as a–c, rather than 1–3, because they could have formed broadly synchronously or they could have formed widely separated from one another in time. Unique relative temporal relations are unconstrained based on the currently available data, and interpretations of temporal relations based on interpretations of crosscutting relations are non-unique, because one would be required to accept assumptions about rheological properties, for example. Labels of 1–3 require robust evidence for unique sequential evolution of the unit members (NASA/USGS Reno Guidelines, 1996, http://planetarymapping.wr.usgs.gov). Although relative temporal relations are not defined, the three members are distinguished on the basis of the structural character as discussed herein. Member a ($rtP_a$), exposed south of Umay-ene Corona, hosts northwest-trending folds and orthogonal (northeast-trending) ribbon troughs. S-C tessera fabrics record local left-lateral shear. Member b ($rtP_b$), which extends west from Umay-ene Corona to the western edge of V–45, hosts northeast-trending fold crests and orthogonal (northwest-trending) ribbon troughs; S-C tessera fabrics record local right-lateral shear. Fold crests in unit $rtP_b$ describe a smooth sweeping curve across the northwestern third of the V–45 map area. The general outcrop pattern of unit $rtP_b$ parallels the fold trends, as do linear flooded basins within unit rtc, all indicative of topographic patterns that mimic the linear fold axis morphology. Artio Chasma is underlain by unit $rtP_b$. Artio Chasma and a parallel ridge to the north host ribbon-fold tessera fabrics that may record non-coaxial shear during ribbon-terrain formation. S-C tessera fabric preserved in both Artio Chasma and the ridge to the north record right-lateral shear across east-northeast-trending shear zones that are approximately 50 to 100 km wide and >500 km long. Member c ($rtP_c$), which lies along the west-northwest-trending high of Pasom-mana Tesserae and hosts west-northwest-trending fold crests and northeast-trending ribbon troughs and S-C tessera fabrics that record local left-lateral shear, divides unit $rtP_b$ into two major packages. Member c ($rtP_c$) is, in turn, divided into two major sections by Zemlika Corona, although parallelism in structural fabric continues from one section to the other. Structural trends in member b ($rtP_b$) could be interpreted as truncating those in member a ($rtP_a$) and appear to be truncated in turn by the structural trends of member c ($rtP_c$). Structural trends of members a ($rtP_a$) and c ($rtP_c$) locally become parallel to one another in the region east of Zemlika Corona, further complicating interpretations of temporal relations. East of Zemlika, structural trends of member c ($rtP_c$) also curve into parallelism with structural trends of unit rtTX.

Tushita and Xi Wang-mu ribbon-tessera terrain (unit rtTX) lies within Tushita and Xi Wang-mu Tesserae. Unit rtTX hosts two different structural fabric patterns that could record a single deformation, or the patterns could provide evidence of two ribbon-tessera formation events. Shields variably developed across the ribbon-tessera terrain units locally obscure both structural trends. Within Xi Wang-mu Tessera, fold axes trend northeast with orthogonally developed ribbon troughs. Within Tushita Tesserae, fold axes and orthogonal ribbon troughs define two suites: (1) fold axes trend northwest on the northwest and southeast parts of Tushita Tesserae; and (2) within central Tushita Tesserae, fold axes trend northeast, parallel to fold axes in Xi Wang-mu Tessera. Ribbon troughs are best developed in the regions with northwest-trending fold crests. Right-lateral S-C tessera fabrics occur within eastern Xi Wang-mu Tessera near the boundary with V–46 at lat 32° S. The ribbon-tessera fabric preserved across Tushita Tesserae represents orthogonal ribbon-fold tessera; no S-C tessera is observed. No clear crosscutting relations between the two fabric trends emerge from detailed mapping; therefore, we map this unit as a single

unit, Tushita and Xi Wang-mu ribbon-tessera terrain (unit rtTX). However, unit rtTX could also be interpreted as two separate units—Tushita ribbon-tessera terrain, marked by northwest-trending fold axes, and Xi Wang-mu ribbon-tessera terrain, marked by northeast-trending fold axes. This interpretation is equally consistent with tessera fabric trends (fig. 4).

Ekhe-Burkhan ribbon-tessera terrain (unit rtE) occurs across the southwestern part of V–45 and extends into V–44 to the west and V–56 to the south. Unit rtE displays a tectonic fabric similar in many ways to orthogonal ribbon-fold fabric (fig. 3), although ribbon troughs represent the dominant fabric element. Ekhe-Burkhan has been defined as a corona (International Astronomical Union (IAU) Working Group for Planetary System Nomenclature (WGPSN)), although as discussed in the section on corona, geologic mapping does not support this interpretation.

Ribbon-tessera terrain also occurs as relatively isolated kipukas within V–45 and, where these kipukas are spatially removed from large tracts of ribbon terrain that inhibit robust correlation with specific ribbon-tessera terrain units, we map the kipukas as a composite unit: ribbon-tessera, undivided (unit rtu).

Structural troughs within both Pasom-mana and Xi Wang-mu tesserae are locally embayed by intratessera basin deposits (unit itb) indicative of flooding late during the formation of the tessera structural fabric (Banks and Hansen, 2000).

We also delineate covered ribbon tessera (unit rtc), exposed across much of the north half of V–45 and surrounding units rtP and rtTX. Unit rtc represents areas across which ribbon terrain fabric elements and trends appear variably masked by apparent burial (fig. 2). We map unit rtc as a single unit because individual units or subunits cannot be identified on the basis of available data, although it almost certainly formed time transgressively given its regional extent and its occurrence around different ribbon-tessera terrains.

### Shield Terrain Materials

Local stratigraphically low ribbon-terrain units are variably covered with an apparently thin veneer of shield terrain. Shield terrain consists of thousands of individual shields and coalesced flow material, referred to as "shield paint" for its apparent low viscosity during emplacement (Hansen, 2005). Shield paint could be formed from any combination of lava flows, air-fall deposits, or pyroclastic flows (Guest and others, 1992; Crumpler and others, 1997). Flooding by this radar-smooth flow material locally highlights gently sloping topographic features that would not normally be visible in Magellan SAR data. Shield terrain contains rocks with an interpreted shared emplacement mechanism (represented by primary structures), which differs from ribbon-tessera terrain whose elements include an interpreted shared deformation history (represented by secondary structures).

Within V–45, shield terrain material (unit s) is marked by extensively distributed small (~1–10 km in diameter) shield edifices and associated local deposits. Unit s generally hosts a higher density of shields than unit rtc although, given that the available SAR data has an effective resolution with respect to shields, individual mapped shields represent a minimum number of shields present—true shield density cannot be robustly determined. Unit s typically lies in contact with the ribbon-terrain units or unit rtc. The contact with the ribbon-terrain units is typically sharp, likely defined by a steep local slope reflecting structural topography of the underlying ribbon-terrain structural topography. In contrast, the contact between units rtc and s is generally gradational, with parallelism of structural trends across the contact. Unit rtc could represent a relatively thin layer of shield-terrain material. The contact of unit s with unit fsu can be sharp to gradational, whereas the contact between units s and fu (composite age, also discussed in the Lowland Basin Flows section) is typically gradational. This relation exists, at least in part, owing to the composite nature of unit fu. Unit s, which is exposed across V–45, almost certainly represents a time-transgressive unit, comprised of thousands of local point-source eruptions that may represent point-source, in situ, partial melting (for example, Hansen, 2005). Unit s almost certainly formed time transgressively across V–45, as has been documented for shield-dominated units elsewhere (for example, Addington, 2001; Hansen, 2005; and Stofan and others, 2005). Unit s could have started to form locally after any local ribbon-tessera unit (rtc, $rtP_a$, $rtP_b$, $rtP_c$, rtTX, rtE, rtu) formed, with unit s forming on that local ribbon-tessera unit. There is no evidence that requires that all unit s formed at one time, or that all of unit s formed after all ribbon-tessera units.

## Flow and Deposit Units

Flow and deposit units across V–45 include three general groups: lowland basin flows and deposits, corona-related flows and deposits, and flows and deposits sourced outside of V–45.

### Lowland Basin Flows

Two lowland basin flow units are defined within V–45 basins: smooth flows, undivided (unit fsu) and flows, undivided (unit fu).

Unit fsu, comprised of radar-dark material, forms isolated exposures generally lying within isolated low topographic basins within the northern half of V–45. Locally, fractures cut unit fsu; parallelism of these fractures with regional fracture suites indicates that the fractures within unit fsu were either locally reactivated, or simply not buried, or some combination thereof. Unit fsu exposed in the northeast corner of V–45 is cut by northwest-trending wrinkle ridges. A parallel suite of wrinkle ridges occurs across much of V–46 (Stofan and Guest, 2003) to the east, cutting so-called "regional plains" units as well as corona-sourced units, such as unit $fCp_a$ (sourced within V–46, but extending into V–45, as discussed in the Flows Sourced Outside of V–45 section). Unit fsu contacts vary from sharp to gradational. Unit fsu, although composite, generally appears to be younger than immediately adjacent units (ribbon-tessera terrain and related units s and fu) on the basis of crosscutting relations. However, it is important to note that this does not require that all of unit fsu formed after all rt and related units. Locally, unit fsu could (but need not) represent a relatively thick deposit of unit s with shield edifices either absent or below effective

data resolution. Unit fsu almost certainly represents a composite unit; it lacks any identified source regions and occurs in basins isolated from one another.

Flows, undivided (unit fu), is a composite unit that occurs within the central and western part of V–45. As its name implies, it consists of many flows and types of flows, including smooth to mottled, lobate to digitate, and variably developed shields, as well as channels. This unit is mapped as a composite unit because the individual materials it contains lack well-defined contacts that can be coherently followed from region to region. Local radar boundaries, marked by differences in radar backscatter character (which may or may not mark unit boundaries), shields, flow directions, and channels shown on the geologic map, provide some indication of the spatial limits of some deposits within unit fu. In general, unit fu has a lower fracture density than locally adjacent units rtc and s, which results from unit fu comprising locally thicker or younger layers (or both) than adjacent portions of units rtc and s. Contacts between unit fu and units rtc and s are generally gradational.

## Corona-related Flows or Deposits

V–45 hosts three flow units (or deposits) associated with coronae within V–45: Zemlika deposit material (unit dZ), Inanna Corona flow material (unit fl), and Codidon, Gurshi, Mou-nyamy flow material (unit fCGM). Each unit occurs in spatial association with the coronae or montes of their namesake, and each is interpreted as genetically related to those features.

Zemlika deposit material is divided into two members, a and b (units $dZ_a$ and $dZ_b$). Member a (unit $dZ_a$) occurs along the rim and exterior, whereas member b (unit $dZ_b$) occurs within the interior. Given that the boundary between these two members is topographic, it is possible that the two members might not represent true material deposits but instead form a single unit. Unit $dZ_a$ is radar smooth and forms an apron around Zemlika; $dZ_a$ is cut by concentric fractures along the rim and an interior slope and by northwest-trending wrinkle ridges locally. Fine fractures that strike northeast also locally cut unit $dZ_a$, although unit $dZ_a$ also truncates (and therefore buries) similarly trending fractures in unit s along its southwest boundary. Unit $dZ_a$ locally forms a relatively low viscosity material that floods structural lows of adjacent ribbon terrain structures in units $rtP_a$, $rtP_c$, and rtTX. Member b (unit $dZ_b$), which lies within the interior of Zemlika, is also radar smooth, although this member hosts numerous shields. Temporal relations between members a (unit $dZ_a$) and b (unit $dZ_b$) are unconstrained.

Inanna Corona flow material (unit fl) is difficult to delineate from its surroundings, although local lobate to digitate flow margins allow us to interpret radial flow outward from central Inanna Corona. Unit fl is best defined east and south of central Inanna Corona, perhaps locally sourced from radial and (or) concentric fracture suites spatially and geometrically (and therefore interpreted as genetically) associated with Inanna Corona. Shields and shield deposits within the central region of Inanna Corona could be associated with shield terrain (unit s), or they could be associated with Inanna flow material (fl); the current SAR data does not allow us to favor one interpretation over the other, although we show unit fl extending as a coherent unit across Inanna Corona.

Codidon, Gurshi, and Mou-nyamy flow material (unit fCGM) forms a composite unit of flows spatially related to Codidon and Mou-nyamy Coronae and intervening Gurshi Mons. Unit fCGM, marked by medium- to low-radar backscatter, preserves faint lobate flow margins indicative of local flow direction. Shields also occur locally, particularly clustered within the central region of the three constructs. The flows locally spill southward into the V–56 map area (Lada Terra) and eastward into V–46, where they correspond to Codidon Corona flow material (unit fCd) and Mou-nyamy Corona flow material (unit fMn) (Stofan and Guest, 2003). We could not clearly identify boundaries between flows associated with each tectonomagmatic construct; therefore, we show this unit as a single composite unit. For example, interpreted flow direction for some flows radiate from Gurshi Mons and, therefore, provide evidence that the flows are likely sourced from Gurshi, yet these same flows are defined as Codidon Corona flow material (unit fCd) in V–46 (Stofan and Guest, 2003). The minor differences between the geologic interpretations of V–45 and V–46 with regard to these flows do not present a significant departure in general interpretations or geologic implications.

## Flows Sourced Outside of V–45

The V–45 map area hosts three flow units with sources clearly outside its boundaries. Ubastet Fluctus and Astkhik Planum flow material (unit fUA), and member 2 of Sephira Mons flow material (unit $fSM_2$) have source areas to the west in V–44, whereas the source of Copia Corona flow material, member a (unit $fCp_a$) lies to the east in V–46 (Stofan and Guest, 2003).

Unit fUA comprises ~300,000 km$^2$ of lobate to digitate, generally radar bright Ubastet Fluctus flow material that radiated to the north, east, and southeast from its source in Astkhik Planum (V–44). Unit fUA spilled into a local broad low in the southwest corner of V–45 (Sezibwa Vallis) where it lapped up on, and flowed around, locally higher outcroppings of unit rtE and across parts of units s and fu, likely post-dating the emplacement of locally adjacent parts of each of these units. Member 2 of Sephira Mons flow material (unit $fSM_2$) also has its source in V–44; this unit forms a summit flow of Sephira Mons, post-dating the emplacement of member 1 of the Sephira Mons flow material (not exposed on this map), and it formed relatively late with respect to unit fUA, which it locally crosscuts (Bridges and McGill, 2002). Unit $fSM_2$ barely extends intoV–45 at ~42° to 44° S., where it flows between local higher-standing exposures of unit rtE and over unit s. Initially we mapped unit $fSM_2$ as part of unit fUA, but we divided these units on the basis of crosscutting relations in the V–44 map area, as defined by Bridges and McGill (2002). Bridges and McGill also delineate digitate plains (their unit pd) along the boundary with V–45 between lat ~42° to 44° S. We found no evidence to delineate two units at this location, and we map this small region as unit $fSM_2$. Bridges and McGill (2002) also map small exposures of tessera (unit t) that match well with the

limits of the unit (as well as structural trends) that we define as Ekhe-Burkhan ribbon-tessera terrain (unit rtE) in this region.

Unit $fCp_a$, which extends into V–45 at the central part of the east boundary, forms a regionally extensive unit sourced from Copia Corona across V–46 (Stofan and Guest, 2003). Our boundaries of unit $fCp_a$ agree well with contact relations defined by Stofan and Guest (2003). Just north of unit $fCp_a$, Stofan and Guest (2003) define a single unit, Aino plains composite material (their unit pcA), along the V–45 boundary. In contrast, we delineate two units—s and fsu—described herein. Unit fsu is clearly younger than unit s at this location, as defined by the sharp truncation of fractures that cut unit s but are buried by material of unit fsu. Unit fsu also shows better development of wrinkle ridges, consistent with the formation of unit fsu as a thin layer (at least locally) formed above an earlier fractured layer below. Given that unit pcA represents a composite unit, interpreted map relations are not in significant conflict along this map boundary. The geologic map of V–46 also shows shields along this portion of the boundary with V–45 (Stofan and Guest, 2003), consistent with the occurrence of unit s, as mapped in this contribution.

Units fUA and $fSM_2$ are not in contact with unit $fCp_a$, nor are they in contact with the flow units associated with V–45 coronae or montes (units $dZ_a$, $dZ_b$, fl, and fCGM) or with composite unit fsu; therefore temporal relations between these units are unconstrained. Each of the flow units are, however, younger than the ribbon-tessera related units and likely younger than at least parts of composite units s and fu.

## Impact Features

Thirteen impact craters, ranging from 9 to 42 km diameter, dot the map area (table 1). Each impact crater displays a rim and ejecta deposit. Seven craters show radar-dark interiors, interpreted as interior flood deposits. Five craters show clear halos, five lack halos, and three occur on units with such a high variation in radar backscatter that we cannot confirm the presence or absence of halos. Impact crater deposits are indicated as crater material, undivided (unit cu), representing ejecta deposits associated with local, time-transgressive, bolide impact. Some impact-crater interiors include a radar-smooth material, interpreted as interior flood deposits (table 1), which is also mapped as unit cu owing to its small areal extent, although the interior fill likely formed after impact crater formation (Izenberg and others, 1994; Phillips and Izenberg, 1995; Basilevsky and Head, 2002; Herrick and Sharpton, 2000). Each impact crater formed during a unique event, therefore, composite unit cu is diachronous across the map area. Crater halos are shown as primary structures rather than as a geologic unit.

None of the craters show obvious signs of embayment by flows that breach the crater rims; however, this relation does not necessarily indicate that the craters lie at the top of the local stratigraphy. Detailed mapping of Venus craters using high-resolution digital elevation models indicates that dark-floored craters with diameter >20 km have an average rim-floor depth of 290 m and rim height (measured from rim to the adjacent surroundings) of 240 m, less than bright-floored craters, indicating significant post-crater volcanic modification (Herrick and Sharpton, 2000; Herrick, 2006; Herrick and Rumpf, 2011). Thus, dark-floored craters likely predate, rather than post-date, the emplacement of at least some of the adjacent units (Herrick, 2006; also see Hansen, 2000, fig. 3, for a possible mechanism). The implication for V–45 is that craters that appear to lie on units rtc, s, fsu, or fu could have formed before the emplacement of these units, and as such the relative age of the craters with these units is effectively unconstrained with the current data. This caution is particularly relevant to craters that lack halo deposits and show flooded interiors; it might also apply to craters that lack halo deposits but are too small to reveal interior flooding given the current data resolution.

The impact craters within the Agnesi quadrangle define two broad groups based on halo and interior deposits—craters that lack halos and show interior flood deposits, as well as craters that have halos and lack interior flood deposits.

Eight impact craters lack halos (or the presence of a halo is indeterminate) and show flooded, or possibly flooded, interiors. Five (Agnesi, Anicia, Kalombo, Lockwood, and Yoshioka) reside on ribbon-tessera units ($rtP_a$, $rtP_b$, $rtP_c$, rtTX, rtE, and rtu) or are adjacent to unit rtc, and three (Lehmann, Masako, and Purev) lie in association with other units. The five craters adjacent to ribbon-tessera units could have formed anytime after the formation of the particular ribbon-tessera unit that they reside next to and before, during, or after the formation of unit rtc (for example, Herrick, 2006; Hansen, 2000, fig. 3). Because ribbon-tessera units could have formed time-transgressively, a crater that lies on top of one ribbon-tessera unit could have formed prior to the formation of another, spatially separate, ribbon-tessera unit. Thus, there is no evidence that requires that all craters formed after all ribbon-tessera units. Craters Anicia and Lockwood show varying degrees of deformation. Northwest-trending fractures locally cut ejecta deposits associated with Anicia crater, as discussed below in the discussion of Mama-Allpa Corona. The fractures likely result from reactivation of previously formed fractures, as it appears that Anicia ejecta both locally covers, and is cut by, fractures. Lockwood ejecta locally embay ribbon-tessera troughs of unit $rtP_a$, and thus provide clear evidence that Lockwood formed after the tessera fabric of $rtP_a$ evolved. However, Lockwood ejecta also appear to be locally cut by fractures that mimic and parallel ribbon-trough bounding structures, likely the result of structural reactivation of earlier formed (that is, pre-Lockwood) ribbon-tessera structures. Given that we have no absolute age constraints, it is equally possible that Lockwood formed late during the formation of the tessera fabric of unit $rtP_a$, or that Lockwood crater formed sometime after the formation of the tessera fabric of unit $rtP_a$ and the tessera structures were reactivated at a later time, unrelated to tessera fabric formation. Relations between Lockwood's ejecta and Zemlika deposit member a (unit $dZ_a$) are unclear, although it appears that channels associated with unit $dZ_a$ may cut Lockwood ejecta; if this is the case, then Lockwood would have to predate the formation of Zemlika Corona. Ejecta deposits associated with Agnesi crater, V–45's namesake, are in contact with flows from Inanna Corona (unit fl), but relative timing between the ejecta and unit fl cannot be determined with currently available data.

Craters Lehmann, Masako, and Purev each show interior flood deposits, and each one either lacks a halo deposit, or the presence of a halo cannot be determined. These craters lie on units fUA, s, and fsu, respectively. Lehmann lies surrounded by unit fUA, sourced in V–44 (Bridges and McGill, 2002). Lehmann's ejecta show an asymmetric distribution with more ejecta on the east and less on the west side of the crater rim. We also interpret isolated deposits (too small to show up on the geologic map) as kipukas of Lehmann's ejecta, using radar brightness and morphology. Based on these observations, we interpret the contact of unit fUA and Lehmann ejecta as one of buttressing by the ejecta. The asymmetric distribution of Lehmann ejecta is consistent with more embayment on the west side of the crater, the direction from which unit fUA was emplaced. These relations indicate that unit fUA formed after the emplacement of Lehmann crater, an interpretation consistent with the lack of a halo due to burial by unit fUA. The reader must be cautious of relative temporal interpretation of craters and surrounding units lacking cross-sectional views. It is our interpretation that unit fUA, which surrounds high-standing ejecta and rim deposits of Lehmann crater, embayed the crater ejecta but did not spill over or breach the crater rim. The interior of Lehmann could have been locally flooded by unit fUA through fissures without breaching the rim (for example, Hansen, 2000; Herrick, 2006; Herrick and Rumpf, 2011). In the case of Masako and Purev, the relative age of the craters and the adjacent unit is indeterminate given relations documented by Herrick (2006); it is possible that the lack of a halo and the presence of interior deposits are due to late emplacement of adjacent units (see also fig. 3 in Hansen, 2000).

Five impact craters (Francesca, Kastusha, Kimitonga, Kosi, and Nomeda) have halo deposits and lack interior flood deposits, consistent with a relatively young age of formation for these five craters (Izenberg and others, 1994; Phillips and Isenberg, 1995; Basilevsky and Head, 2002; Herrick and Sharpton, 2000). Craters Kosi and Nomeda lie on unit fCGM, indicating that this composite unit predated formation of these craters. Given the composite nature of unit fCGM, it is possible that portions of the unit post-dated crater formation, although this cannot be determined based on the current data. Francesca, Kastusha, and Kimitonga are surrounded by unit fsu, likely indicating that composite unit fsu at these locations pre-dated formation of these three craters, given the preservation of crater haloes and the lack of interior flooding.

## Tectonic Structures

Both local and regional tectonic structures occur across Agnesi quadrangle (V–45). Local structural patterns are generally areally confined to or geometrically associated with individual features such as coronae. Regional structures describe coherent patterns across larger areas and lack spatial or geometric correlation with individual features. The timing of local structures likely corresponds to the formation, or stages of formation, of the individual features with which they are associated. Temporal evolution of regional tectonic structures (1) is difficult to constrain, (2) may be time transgressive, and (or) (3) may involve reactivation (for example, DeShon and others, 2000). Regional structures in V–45 include regional fractures and wrinkle ridges. Ribbon-tessera fabrics and structures associated with individual geomorphic features are not considered regional structures herein. Ribbon-tessera fabrics are described above in the section on tessera terrain, and local structures associated with individual geomorphic features are discussed with individual features in the next section.

### Regional Extensional Structures

Regional fractures display a coherent pattern across the northern two thirds of V–45, generally striking north-northeast in the west and gradually changing to an east-northeast strike in the east. These lineaments, which are likely comprised of composite fractures with collective lengths >1,000 km, are interpreted as extensional fractures based on their straight sharp character and lack of notable topographic expression or along-strike offset. Fractures shown on the geologic map indicate the general trend and character of the fracture suite; however fracture spacing, 1–2 km or less (locally down to the resolution of the current SAR data set), is too detailed to show on the 1:5-million-scale geologic map. Extension fractures, best preserved in local topographic highs, are both locally covered by and cut material of units rtc and s, indicating that the fractures were formed and (or) reactivated through time. Although the fractures generally describe a northeast trend, locally fractures mimic local topography and geometry of individual geomorphic features, indicating that some fractures formed (or were reactivated) in association with individual features.

Locally, fractures trend parallel to the ribbon trends of nearby ribbon-tessera units, likely representing reactivation of earlier-formed ribbon structures.

Notably, regional fractures, over 1,000 km in composite length, trend in a northeast direction along the northwest boundary of both V–45 and V–44. These fractures lie parallel to and their extensions coalesce with regional fractures in V–44 (Bridges and McGill, 2002).

### Wrinkle Ridges

Wrinkle ridges define low sinuous spines, spaced a few kilometers apart and up to a few hundred kilometers long, found on most terrestrial worlds, especially on large flat expanses of volcanic flow materials (Watters, 1988). Wrinkle ridges, which are sparsely developed within V–45, trend northwest across the northeast part of the map area. Like the fractures, wrinkle ridges occur at a range of spacing, down to small-scale wrinkle ridges too closely spaced to show on the 1:5-million-scale geologic map. Wrinkle ridges are notably absent within exposures of ribbon-tessera terrain, even in high-resolution images although wrinkle ridges can occur right up to the contact between ribbon-tessera terrain and shield terrain. These relations suggest that ribbon-tessera terrain is not rheologically amenable to wrinkle ridge formation (that is, it lacks a thin deformable layer), whereas the thin shield-terrain veneer readily forms wrinkle ridges. Thus, the presence or absence of wrinkle ridges in this

case is likely related to rheological criteria rather than temporal considerations.

## Geomorphic Features

V–45 includes one chasma, ten coronae, and two montes.

### Artio Chasma

Artio Chasma forms a paired ridge-trough-ridge feature that is approximately 100 km wide and 1,000 km long. The higher northern ridge reaches a height of 6,052.3 km, whereas the trough lies as deep as 6,051 km. Artio extends northeast from (and includes) Inanna Corona to Pasom-mana Tesserae. Artio hosts ribbon-tessera fabric of unit rtP; folds parallel the trend of Artio, as well as the ridges and trough. Artio differs from many chasma on Venus in that it (1) does not lie along the topographic boundary of a singular corona, or numerous coronae, (2) it is relatively shallow, and (3) it is spatially and structurally associated with ribbon-tessera terrain. Artio has as much in common with some dorsa, as it does with chasmata on Venus, given the topographic ridges that parallel the topographic trough. The evolution of Artio was likely greatly influenced by the ribbon-tessera fabric that cores the feature. Tessera terrain fold axes parallel the long-wavelength ridges and trough of Artio Chasma. A second wider ridge (approximately 200-km wide) parallels Artio to the north. This ridge lacks a geographic label, although it, like Artio, hosts parallel ridges and troughs that also parallel the feature's trend. The northern curvilinear ridge also hosts ribbon-tessera fabrics with ridge-parallel fold axes. An approximately 100-km-wide linear low separates Artio and the northern ridge; both features curve into Pasom-mana Tesserae to the east.

### Coronae and Montes

V–45's ten lowland coronae and two montes (table 2) represent a relatively large number of coronae and montes compared to other Venus 1:5-million-scale quadrangles situated away from coronae chains. The coronae and montes within V–45 range from 75 to 600 km in diameter. Spatially they do not define obvious chains or clusters, nor are they particularly isolated from one another. Each corona and mons, with the exception of Codidon and Mou-nyamy Coronae and Gurshi Mons (southeast corner of V–45), occur adjacent to lowland ribbon-tessera terrain.

The coronae and montes represent four different geomorphic styles. Quasi-circular domes mark four of the coronae (Inanna, Codidon, Mou-nyamy, and Elihino), whereas circular basins mark five others (Mama-Allpa, Umay-ene, Xcanil, Zemlika, and Pakoti). The domical coronae (termed lowland radial coronae, herein) show well-defined radial fractures and less-defined concentric fracture suites, whereas the basinal coronae (termed circular lows, herein) show well-defined concentric fractures but lack radial features. Gurshi Mons (southeast corner of map region), which displays radial fractures, looks morphologically similar to the nearby lowland radial coronae, Codidon and Mou-nyamy. Centrally located Tuzandi Mons also displays radial fractures that modify the underlying ribbon-tessera terrain upon which it is built. A third, previously unrecognized corona, located south of Zemlika Corona and defined by both radial and concentric fractures, appears morphologically similar to the other lowland radial coronae and montes within V–45. Ekhe-Burkhan Corona (southwestern V–45) differs morphologically from the lowland radial coronae and the circular lows. Each corona/mons is briefly described in the following sections in geographic order, starting with Mama-Allpa in the northwest corner of V–46 and proceeding in a general clockwise sense.

#### Mama-Allpa Corona

Mama-Allpa Corona (300 km in diameter; lat 27° S., long 31° E.), which lies in the northwest corner of V–45, represents perhaps the most complex of the coronae/montes features within V–45. Mama-Allpa straddles the boundary with V–44 to the west. Geologic mapping of Mama-Allpa required considering high-resolution SAR and altimetry centered on the feature owing to complications of pre-existing ribbon-tessera terrain and young fracture formation, which included structural reactivation as well as impact crater formation. At first glance Mama-Allpa appears to be defined by complex fracture patterns, including fractures that might be interpreted as radial; however, detailed mapping allows delineation of geologic elements in time and space, and, thus, a different picture of Mama-Allpa emerges.

A circular topographic ridge, marked by locally buried concentric fractures, defines Mama-Allpa. The interior lies just below 6,051.8 km and hosts numerous small shields that likely locally bury additional concentric fractures. The area surrounding Mama-Allpa hosts earlier formed ribbon tessera (unit rtu), which is locally covered (unit rtc) and fractured. Mama-Allpa, a circular basin, is delineated by two nested concentric structures marked by subtle topography, RMS slope values, and subtle concentric structures. Geologic mapping reveals three or four general patterns of fractures within the region surrounding Mama-Allpa. These patterns are (1) fractures parallel to local ribbon-tessera trends, with fractures parallel to both ribbon and fold elements; (2) fractures concentric to Mama-Allpa marking nested concentric suites; (3) north- and northeast-trending regional fractures that occur across an area significantly larger than Mama-Allpa; and (4) a population of possible radial fractures centered east of Mama-Allpa Corona. In addition, impact crater Anicia lies along the northeast rim of Mama-Allpa, post-dating the formation of Mama-Allpa as indicted by the sharp topographic truncation of the Mama-Allpa ridge and adding to the complexity of unraveling the geologic history of the area around Mama-Allpa. Ejecta deposits associated with Anicia crater appear locally cut by northwest-trending fractures—these relations represent either (1) reactivation of earlier (pre-impact) fractures, as ejecta deposits clearly truncate and bury fracture trends or (2) formation of post-impact fractures possibly centered just east of the Mama-Allpa structure. Despite the complexity of Mama-Allpa, we found no evidence of radial fractures or radial flows associated with the Mama-Allpa structure. A suite of possible radial fractures occurs to the east

of Mama-Allpa Corona (4 above), although these fractures may represent serendipitous interaction of unrelated fractures, rather than true genetically related radial fractures. No unique material map units associated with Mama-Allpa Corona were recognized in the SAR data.

Northeast to east-central V–45 hosts three circular geomorphic features, from north to south. These features are Umay-ene Corona (370 km diameter; lat 27.5° S., long 50.5° E.), Zemlika Corona (150 km diameter; lat 33.5° S., long 50° E.), and Elihino Corona (370 km diameter; lat 37° S., long 49° E.). Umay-ene and Zemlika represent circular basins that lack radial structures, whereas Elihino Corona defines a subtle domical structure defined by radial and concentric structures and which emerged as a result of geologic mapping.

Umay-ene Corona is defined topographically as well as structurally; it lacks obvious volcanic features other than numerous shields developed within its interior basin. Topographically, two nested ridges lie centered about the central basin. Concentric fractures parallel the outer of the two broad ridges. Shield terrain, unit s, appears to blanket the region of Umay-ene, although it is unclear if Umay-ene formation pre-dated, post-dated, or evolved synchronously with, the development of the unit s surface. Unit s, spatially associated with Umay-ene, hosts northwest-trending wrinkle ridges on Umay-ene's southeastern inward facing slope. These wrinkle ridges are similar in form and trend to, though significantly more closely spaced than, regional wrinkle ridges developed in northeastern V–45. The wrinkle ridges likely post-date most, if not all, of Umay-ene's formation. Regional wrinkle ridges (parallel in trend) formed after east-northeast-trending fractures and after emplacement of a local thin surface cover (unit s). Shields, wrinkle ridges, and northeast-trending extension fractures variably occur spatially associated with Umay-ene. Ribbon-tessera terrain units $rtP_a$ and $rtP_b$ lie to the west of Umay-ene. Umay-ene formed after adjacent ribbon-tessera terrain as indicated by truncation of ribbon-tessera fabric trends by Umay-ene. Isolated kipukas of ribbon tessera occur to the north, southeast, and east of Umay-ene, indicating that Umay-ene likely formed on or across earlier formed ribbon-tessera terrain. No ribbon-tessera fabric has been recognized within Umay-ene. Shields dominate Umay-ene's interior basin. Concentric fractures formed synchronously with, and are likely genetically related to, Umay-ene basin formation. There is no evidence that radial fractures formed at any time during Umay-ene evolution; if radial fractures had formed after Umay-ene evolution, we would expect to see radial fractures cutting adjacent unit rtP fabrics, and they should also affect the formation of regional fracture and wrinkle-ridge patterns, which is not the case. If radial fractures formed before regional fractures, then we would expect regional fractures to have been affected by the presence of the radial fractures. If radial fractures formed after regional fractures (and therefore after unit s), then radial fractures should be clearly preserved.

Zemlika Corona represents a rimmed, 150-km-diameter, 1-km-deep, circular basin. Delicate, closely spaced concentric fractures and pit chains decorate the 0.5-km-high rim and inner basin slope. The presence of the pit chains likely indicates that subsurface magma accompanied Zemlika evolution. Unit $dZ_a$ forms a radar-smooth apron surrounding Zemlika, and it includes material that floods structurally defined topographic lows within the adjacent ribbon tessera, unit rtP. Unit $dZ_a$ likely underlies the rim and possibly the interior region. Unit $dZ_b$, comprised of flows and shields, occupies the interior basin. Local northwest-trending wrinkle ridges, parallel to regional wrinkle ridge trends, cut Zemlika's apron of unit $dZ_a$ to the north and south. Zemlika is almost completely surrounded by ribbon-tessera terrain; earlier-formed tessera fabrics of rtP members a and c, marked by orthogonal ribbons and folds, show no evidence of disruption by Zemlika, except that the tessera fabrics are abruptly truncated in cookie-cutter fashion by Zemlika. These relations indicate that Zemlika must have formed after unit rtP acquired its characteristic fabric.

As with Umay-ene, Zemlika's evolution did not include the formation of radial fractures; if radial structures had formed with the evolution of Zemlika, they would be preserved in the tessera fabric. Temporal relations among units $dZ_a$, $dZ_b$, and composite unit fu are unclear, although northeast-trending fractures that cut unit fu appear truncated along strike at the fu-dZ contact, consistent with post-fracture emplacement of unit $dZ_a$, and, by extension, the evolution of Zemlika Corona. As noted above, Lockwood crater post-dates (or overlaps with) the formation of unit $rtP_c$, but the relative timing with respect to unit $dZ_a$ is unconstrained.

South of Zemlika, fracture patterns define a previously unrecognized quasi-circular (planform) feature, Elihino Corona. On the basis of both geologic and geomorphic features, we suggest that this feature should be considered a coronae. Elihino Corona, defined by both radial and concentric fractures, is also marked by a slight domical interior and quasi-circular trough along its north margin. Shields cluster within its topographically and structurally defined interior. Elihino Corona lacks obvious radial flows, although shields and associated deposits clearly bury, and therefore post-date, the formation of neighboring ribbon-tessera terrain units rtTX and rtc. Northeast- and southwest-striking fractures that radiate from central Elihino Corona parallel regional fractures. Southeast-striking radial fractures parallel ribbon-tessera fabrics to the south. The bulk of Elihino Corona lies within unit rtc; the radial and concentric patterns of fractures may indicate that the earlier formed rtc surface (and adjacent units fu and s, to the northeast and southwest, respectively) was domed and fractured from below during the formation of Elihino Corona.

## Codidon Corona

Codidon Corona (250 km diameter; lat 46° S., long 56° E.) lies in the southeast corner of V–45 together with Gurshi Mons (210 km diameter; lat 47.5° S., long 58.5° E.) and Mou-nyamy Corona (200 km diameter; lat 49.5° S., long 59° E.). These three features form domical tectonomagmatic features, and each one is marked by radial structures and subtle radial flows. Codidon Corona also hosts concentric structures. The radial structures of all three features generally form fine fractures. Flows coalesce in such a way that it is difficult to interpret relative temporal timing between flows and, by extension, individual flow sources and the relative temporal development of each of these three features. Radial fractures centered on Gurshi Mons, which lies

between the other two features, curve outward toward Codidon Corona to the north and Mou-nyamy Corona to the south, suggestive of broadly synchronous development of all three features. In any case, no obvious crosscutting relations occur among the three features. Composite flows spill eastward and southward into adjacent quadrangle regions V–46, V–56, and V–57. Shields occur in association with all three tectonomagmatic features, commonly clustered near their topographic centers and the convergence of their radial structures. Shields also occur away from these central regions. These three features formed after unit rtTX acquired its tessera fabric as indicated by local burial of unit rtTX structural fabrics by corona- and mons-associated flows (unit fCGM). These three tectonomagmatic features also likely dominantly post-date the formation of unit s in this region, although such temporal relations are less robustly constrained. Impact craters Kosi and Nomeda, each with halo deposits, formed after the formation of Codidon, Gurshi, and Mou-nyamy; both impact craters overlie unit fCGM.

### Ekhe-Burkhan Corona

Ekhe-Burkhan Corona lies within southwesternmost V–45, extending westward and southward into V–44 and V–56. Ekhe-Burkhan Corona is the largest of the geomorphic features discussed herein. In addition to its large size, Ekhe-Burkhan Corona differs from the other coronae and montes on the basis of (1) its plateau-like form, (2) its structural fabric akin to ribbon-tessera terrain (Hansen and Willis, 1996, 1998), (3) its lack of a well-defined boundary or limit, and (4) its lack of a clear circular planform pattern based on topography and secondary structures. We do not consider this feature either a corona or a mons, although it is discussed here because Ekhe-Burkhan Corona is its formal given name. The International Astronomical Union defines a corona as an "ovoid-shaped feature," so Ekhe-Burkhan Corona retains its formal geographic name and is labeled as such on the map; however, in our interpretive discussion we refer to this feature as Ekhe-Burkhan Corona feature, because the feature does not meet the geologic definition of a corona.

Ekhe-Burkhan Corona feature, marked by a tectonic fabric with orthogonal fine-scale (penetratively developed) folds and ribbons (fig. 3), includes a quasi-circular ridge with a diameter of about 600 km, although the feature itself extends at least a diameter beyond this ridge in all directions for which Magellan SAR data exist. Thus, Ekhe-Burkhan Corona feature might be >1,200 km in diameter, and as such it would be the largest corona on Venus (note, Artemis with a diameter of ~2,500 km is no longer considered a corona [for example, Stofan and others, 1997, 2001; Hansen and others, 1997; Hansen, 2002; Bannister and Hansen, 2010]). We map the fabric of Ekhe-Burkhan as ribbon-tessera terrain, unit rtE. Within V–44 (Kalwin quadrangle) to the west, unit rtE is mapped as tessera terrain (Bridges and McGill, 2002). Units s and fu locally bury, and therefore post-date, the formation of the structural fabric that characterizes Ekhe-Burkhan, unit rtE. Similarly, flows sourced from V–44, unit fUA, also bury and hence post-date, the formation of unit rtE. Kipukas of unit rtE lie within each of these three units; the continuity of fabric orientation between and among isolated kipukas of unit rtE indicates that unit rtE likely underlies a vast region, including that of Tuzandi Mons, discussed in the following section.

### Tuzandi Mons

Tuzandi Mons (200 km diameter; lat 42.5° S., long 41.5° E.), which lies in south central V–45 northeast of Ekhe-Burkhan Corona feature, represents a domical feature decorated with closely spaced radial structures. Tuzandi Mons is morphologically similar to Gurshi Mons and Mou-nyamy Corona, although its surface is mapped as units rtE and s. Radial structures characterize unit rtE at this location; variably developed shields and associated deposits (unit s) locally cover unit rtE. We did not recognize any flows that could be uniquely attributed to the formation of Tuzandi Mons, such as obvious radial flows sourced from central Tuzandi Mons. It is possible, however, that such flows exist but simply cannot be unequivocally identified with currently available data. Local radar boundaries that might represent parts of lobate flows sourced from Tuzandi Mons are indicated on the geologic map. The topographic signature of Tuzandi Mons formed late, but perhaps synchronously, with respect to the evolution of the tectonic fabric of unit rtE, and it could have formed broadly synchronously with time-transgressive unit s. Numerous shields occur in and around Tuzandi Mons, although their genetic association to Tuzandi Mons is unclear. Based on the geologic and geomorphic character of Tuzandi Mons described above, this feature seems better classified as a corona.

### Inanna Corona

Inanna Corona (350 km diameter; lat 37° S., long 35.9° E.), an elongate dome-like feature marked by concentric ridges, suites of radial and concentric fractures, and possible radial flows, lies in the west-central part of V–45. Central Inanna Corona lies topographically below the concentric ridges that define Inanna, but not below the surrounding region. The northern boundary of Inanna Corona lies along the westernmost extent of Artio Chasma. Subtle flows, interpreted as sourced from Inanna Corona in this study, extend radially outward to the south into the adjacent lowland. Shields cluster in central Inanna as well as along its northern and western boundaries. As with the other V–45 coronae and montes that are marked by radial fractures, the spatial limit of Inanna Corona is not well defined. In terms of temporal evolution, Inanna Corona clearly formed after units rtP, rtu, and rtc, given that flows interpreted as associated with Inanna Corona locally flood structural topography associated with the characteristic structural fabric of units rtP, rtu, and rtc. Temporal relations between the evolution of Inanna Corona and units s and fu are less clear and could have broadly overlapped in time.

### Xcanil Corona

Xcanil Corona (150 km diameter; lat 37° S., long 43° E.), which lies almost due east of Inanna Corona, marks an approximately 1-km-deep circular basin, or so-called circular low, decorated with delicate concentric fractures. Two, apparently

distinct fracture suites, each seemingly formed by the reactivation of ribbon-tessera structures, intersect in the center of Xcanil. A third, north-trending fracture suite may locally reactivate north-trending ribbon structures. Local flows cover the fractures and hence post-date fracture formation, but the flows are also cut by some fractures within the fracture suites, indicative of broadly synchronous formation of flows and fractures and likely structural reactivation of previously formed fracture suites. Small local possible exposures of unit rtP (too small to show on the map) show tessera-fabric trends parallel to tessera-fabric trends of unit rtP elsewhere, consistent with the interpretation that unit rtP lies buried at shallow depth locally. Local preservation of kipukas of unit rtP, so close to (and possibly within the interior of) Xcanil, would seem to require that parts of the pre-existing surface were preserved during and by the process that led to the formation of Xcanil, which would presumably limit genetic mechanisms to endogenic or subsurface processes and rule out exogenic processes in the case of Xcanil. Xcanil also lacks radial fractures, and therefore processes that would result in the formation of radial fractures could not have contributed to the formation of Xcanil. Shields occur both within and around Xcanil, locally burying fractures. Xcanil lies along an east-northeast-trending ridge that parallels Artio Chasma to the north. Xcanil forms on unit rtc, generally having formed broadly synchronously with, or possibly after formation of, unit rtc.

### Pakoti Corona

Pakoti Corona (75 km diameter; lat 38° S., long 42.5° E.) lies approximately 100 km south of Xcanil Corona. Like Xcanil Corona, Pakoti Corona represents a circular basin, or so-called circular low, decorated with concentric fractures. Given the similarity of these two features, we suggest that Pakoti Corona should be classified as a corona. A northeast-trending fracture suite crosses Pakoti Corona, which lies completely within unit s. Shields both cover, and are cut by, concentric and northeast-trending fractures. Like Xcanil, Pakoti lacks any evidence that radial fractures accompanied the formation of this feature. The topographic signature of Pakoti Corona is similar to that of Agnesi crater.

## Geologic History

The geologic history that emerges from this geologic mapping effort is relatively simple at a long-wavelength time scale, although it is also likely quite rich at a local (short-wavelength) time-space scale. Basal ribbon-tessera terrain units clearly formed across V–45 in a time-transgressive manner, including the formation of the tectonic fabric of units rtP, rtTX, rtE, and rtu, and the units itb and rtc. Basal unit formation was accompanied, or followed, by local formation (not necessarily at the same time) of circular low features (Mama-Allpa, Umay-ene, Zemlika, Xcanil, and Pakoti) and radial coronae Inanna, Elihino, and Tuzandi Mons, all of which lie surrounded by ribbon-tessera terrain. The relative temporal relations among these features are unconstrained. Extensively developed shield terrain evolved time-transgressively coupled with the formation of the coronae and montes features and formation and reactivation of regional fractures. Shield-terrain formation could have locally overlapped in space and time with the formation of these coronae and montes, perhaps forming locally before some of these features and certainly continuing to form after the evolution of individual coronae and montes. The evolution of units fu and fsu, which represent composite time-transgressive units, are similarly poorly constrained in both time and space. The timing of the formation of Codidon and Mou-nyamy Coronae and Gurshi Mons in southeastern V–45, the emplacement of associated flow material, and the evolution of related radial and concentric fracture suites are unconstrained; however, the coronae and montes formed after unit rtE acquired its tectonic fabric, as evidenced by embayment of corona- and mons-related flows into local structural topography of the unit rtE fabric. As noted, relative temporal formation between each of the coronae and montes is unconstrained, although fracture and flow relations seem most consistent with broadly synchronous development of these three features. Flows from outside the boundaries of V–45, both from V–44 and V–45, were emplaced relatively late in the history of V–45. Ubastet Fluctus and Sephira Mons flow material locally embayed V–45 from the west, whereas flows from Copia Corona locally embayed V–45 from the east. Wrinkle ridge structures (limited to the northeast corner of V–45) also appear to have formed relatively late; wrinkle ridges could also have formed time-transgressively (for example, McGill, 2004), although they show a consistent northwest trend across different material units, including units s, fsu, and $fCP_a$, units that each formed at different times. The simplest history is one in which the various units are emplaced through time, and wrinkle ridges form across those units that are rheologically suited to wrinkle ridge development at some point after each of the affected units was in place. This simple history would imply that wrinkle ridges within this area formed within a single temporally limited event and that the event occurred after (or during) the formation of the various units that are deformed by wrinkle ridge structures.

The orientation of the wrinkle ridges within V–45 provides a likely clue to their formation. Based on orientation, wrinkle ridges in V–45 are part of a much larger suite of concentric wrinkle ridges with a diameter of ~13,000 km, associated with the formation of Artemis Chasma (Hansen and Olive, 2010). New regional geologic mapping (Hansen and Olive, 2010) reveals that concentric wrinkle ridges and radial fractures together define a coherent pattern centered on Artemis Chasma located in V–48 (Bannister and Hansen, 2010). The wrinkle ridges in V–45 broadly parallel those in V–46 (Stofan and Guest, 2003) to the east. The northeast corner of V–45 represents the southwestern limit of Artemis. Because V–45 preserves the apparent spatial limit of the Artemis wrinkle ridge suite in this area, we cannot use the presence (or absence) of wrinkle ridges to provide temporal constraints with units elsewhere within V–45. Hansen and Olive (2010) document that Artemis and the 13,000-km-diameter suite of wrinkle ridges post-date the formation of ribbon-tessera terrain units (Hansen

and Lopez, 2010) that lie within the spatial limits of broadly defined Artemis Chasma.

It is worth noting that within northeast V–45 local units s, fsu, and $fCp_a$ broadly post-date the formation of rtTX, $rtP_a$, and $rtP_c$. However these rt units are not deformed by wrinkle ridge structures, a fact which clearly indicates the rt units were not mechanically amenable to wrinkle ridge formation.

Unit fCGM shows limited development of short wrinkle ridge features. Although the orientation of these wrinkle ridges is the same as would be expected if these structures were part of the Artemis wrinkle ridge suite, the limited development of the structures leaves the correlation an open question. Thus on the basis of geologic relations presented here, the relative timing of the formation of unit fCGM and the Artemis wrinkle ridge suite is unconstrained. However, correlation of unit fCGM with adjacent units in V–46 (Stofan and Guest, 2003) to the east would suggest that wrinkle ridge formation post-dates this unit.

Although the formation of the various ribbon-tessera fabrics appears to pre-date the formation of the coronae and montes, specific relative temporal relations between the formation of individual ribbon-tessera terrain units and the evolution of individual coronae and montes are essentially unconstrained. The lack of robust temporal constraints should not, however, be taken as evidence that (1) all the tessera terrain formed at the same time, (2) all the coronae and montes evolved synchronously, or (3) all tessera terrain fabric formed before all coronae/montes.

Ribbon-tessera terrain units across the northern part of V–45 record crosscutting relations, providing evidence that these units do not represent a single temporal event. Detailed geologic histories and implications of these histories are discussed in the three following sections.

## Implications for Lowland Ribbon-Tessera Evolution

Geologic mapping of the Agnesi quadrangle (V–45) provides an opportunity to examine the nature of lowland ribbon-tessera terrain, as compared to highland ribbon-tessera terrain. Ribbon-tessera terrain, a structurally distinctive terrain marked by generally orthogonal fold axes and ribbon troughs (Hansen and Willis, 1996, 1998) generally characterizes Venusian crustal plateaus, although this distinctive fabric is also variably preserved across some lowland regions, including the Agnesi quadrangle.

Venus' S-C tessera terrain, which records deformation at the surface, shows a ductile character as noted by many workers (Hansen, 1992, 2006; Hansen and Willis, 1996; Ghent and Tibuleac, 2002; Tuckwell and Ghail, 2003; Kumar, 2005; Romeo and others, 2005). In the case of crustal plateaus, entire crustal plateau surfaces are commonly characterized by ductile character of deformation fabrics, as well as kinematically coherent brittle deformation; these observations indicate that the surface deformed simultaneously in both brittle and ductile modes (Hansen, 2006). Rocks can deform in this fashion at mid-crustal levels on Earth, but they do not deform in this manner on the surface of the Earth. In general, away from crustal plateaus, rocks at Venus' surface deform quite similarly to rock at Earth's surface. Despite the much higher surface temperature on Venus, which might allow rocks to deform through ductile processes such as viscous creep, Venusian rocks are quite strong as a result of their extremely dry state (Mackwell and others, 1998). However, the nature of the deformation fabric appears unique within Venusian crustal plateaus and inliers of ribbon-tessera terrain, such as within V–45. What makes these regions unique is the uniformly ductile character of their deformation patterns. The very fact that we can recognize coherent tectonic patterns over huge areas provides a clue to the surface evolution. This continuity in structural pattern results from ductile deformation and indicates that over these huge areas, covering several millions of square kilometers, Venus' surface deformed in a ductile fashion. Although tessera-terrain fabrics show a range of characteristic fabrics, each of these fabrics shares evidence of ductility (see Hansen and Willis, 1996, their fig. 3). Hansen (2006) proposed that ribbon-terrain fabric ductility reflects the extremely hot environment of crustal plateau tessera-terrain formation in the past, resulting from progressive deformation and solidification of huge lava ponds representing individual crustal plateaus, an interpretation consistent with thermal modeling of ribbon structures (Gilmore and others, 1998; Ruiz, 2007). This interpretation appears applicable to lowland ribbon-tessera terrain preserved across much of V–45.

For the purpose of discussion, we divide V–45 ribbon-tessera terrain into two regional groups—northern tessera and southern tessera. Tessera outcrops, marked by penetratively developed tectonic fabrics, occur at the highest altitudes, and they likely represent the oldest local deformation. The northern tessera host well-defined ribbon and fold fabrics typical of ribbon-tessera terrain preserved in crustal plateaus, including orthogonal ribbon-fold fabrics and S-C tessera fabrics. The southern tessera terrain hosts a similar, but possibly different, fabric. The northern tessera-terrain ribbons and folds describe regional patterns coherent over hundreds of kilometers, yet the patterns show apparent truncation by one another as noted (fig. 4). Unit rtc occurs around much of the northern tessera; lineaments within unit rtc typically parallel the trends of adjacent tessera structural patterns, and unit rtc typically hosts numerous small shields, forming a thin veneer above tessera terrain.

The southern tessera, which occurs most extensively in the southwest corner associated with Ekhe-Burkhan Corona feature, crops out as kipuka among flows of Sezibwa Vallis and among numerous shields in the region surrounding Tuzandi Mons and locally includes tectonic fabrics that appear to be similar to orthogonal ribbon and fold fabrics, but elsewhere the tectonic fabric is more complex. A penetrative radial fabric marks Tuzandi Mons as reminiscent of tessera terrain and some coronae, as well as the tectonomagmatic centers preserved within the interior of Artemis (V–48; Bannister and Hansen, 2010). Patterns within the tessera tectonic fabric can be traced between adjacent outcrops or kipukas, as well as across Tuzandi Mons. Tuzandi Mons may have formed synchronously with the local radial fabric. The southern tessera likely record an extensive history including initial formation of the tessera tectonic fabric, local burial by shields, cutting by regional structures, continued

local burial by shields, and structural reactivation of pre-existing structures with optimum orientation.

The northern and southern tessera terrain within V–45 show different regional patterns as recorded in their tectonic fabrics, and as such there is no reason to suggest that these two groups of units formed synchronously. In addition, the northern package of tessera terrains clearly records crosscutting relations (which is different than clear crosscutting relations), indicating that these various units and perhaps unit members did not form at the same time geologically—that is, the units record a history and an evolution. This point is important because it means that detailed mapping and analysis of ribbon-tessera terrain has the potential to unravel a rich geologic history of the evolution of these various terrains, which in turn can lead to an understanding of the operative environmental conditions during the evolution of these terrains, as well as an understanding of the planetary process(es) responsible (for example, Gilbert, 1886).

It is possible that the various ribbon-tessera terrain units and (or) members could record progressive solidification and deformation of the scum of a huge lava pond, or more than one lava pond (for example, Hansen, 2006), that formed across much of the region now present within V–45. S-C ribbon-tessera fabric could represent localized shear zones formed as a result of relative horizontal translation of rafts of lava pond scum. The formation of the circular lows and the radial coronae that lie in close proximity to ribbon-tessera terrain within V–45 might also record relatively early evolution of ribbon-tessera-terrain surfaces, or they might have formed (individually or collectively) as a result of events completely unrelated to ribbon-tessera terrain evolution.

The circular lows of Mama-Allpa, Umay-ene, Zemlika, and Xcanil Coronae clearly crosscut adjacent tessera-terrain topography and tectonic fabric. Inanna and Elihino Coronae, which represent the radial coronae family, occur in close proximity to ribbon-tessera terrain and clearly post-date local tessera fabric formation. Radial coronae/montes Codidon and Mou-nyamy Coronae and Gurshi Mons are spatially separate from the tessera, and as such temporal relations are less certain; however, it appears that these features likely post-date tessera formation or formed late in the evolution of ribbon-tessera terrain. In contrast, Tuzandi Mons could have formed contemporaneously with southern tessera (unit rtE), as noted. Another critical observation may be the sharp topographic demarcation of the basinal circular low features (topographically and tectonically), which stands in strong contrast to the gradational character typical of the radial domical coronae. These geomorphic differences might be most easily reconciled if circular lows and radial coronae formed by different unrelated processes. Radial coronae likely represent endogenic evolution (for example, Stofan and others, 1992, 1997), whereas circular lows could record endogenic or exogenic evolution. If some circular lows formed by endogenic processes, they may record a different endogenic process than that responsible for the formation of radial coronae. These topics are discussed briefly in the following section.

# Implications For the Formation of Coronae and Montes

As noted, V–45 provides an excellent opportunity to examine the formation of lowland coronae and montes. Lowland coronae are relatively rare (10 % of coronae; 50–55 total); therefore coronae in V–45 represent about 20 percent of all lowland coronae. Lowland coronae typically form isolated features—that is, not occurring in chains or clusters, as do most coronae (Stofan and others, 2001). The evolution of coronae, whether by a single mechanism or a range of mechanisms, is a topic of debate (for example, Stofan and others, 1992, 2001; Vita-Finzi and others, 2005; Hamilton, 2005), and lowland coronae, in particular, may provide critical clues to coronae evolution.

Geologic mapping allows us to divide the coronae and montes into four geomorphic groups (features A–D) on the basis of (1) planform shape (topographic form, for example, dome versus basin), (2) structural character (radial versus concentric structures), (3) ellipticity, and (4) associated deposits, presumably mostly volcanic in nature (table 2). Features A (Codidon, Inanna, Mou-nyamy, and Elihino Coronae) are domical structures with ellipticity <0.75, radial fractures, and variably developed (or preserved) radial flows; these features show variably developed concentric structures, including ridges and (or) concentric fracture suites. Features B, Gurshi and Tuzandi Montes, share most characteristics of features A, except that they are more circular in planform, and they lack concentric structures. We consider features A and B similar to one another. Features C (Mama-Allpa, Umay-ene, Xcanil, Zemlika, and Elihino Coronae) are basinal structures, with nearly circular planform (ellipticity >0.85); they are decorated with concentric structures, and they lack evidence for radial structures and (or) radial flows. We call these features “circular lows” (for example, Hansen, 2008; Lang and Hansen, 2008; McDaniel and Hansen, 2005). Feature D, Ekhe-Burkhan Corona feature, differs from the other features with its plateau-like form, its structural fabric akin to ribbon-tessera terrain (Hansen and Willis, 1996, 1998), and its lack of well-defined circular boundaries or limits.

On the basis of these observations, we suggest a reclassification of these features within V–45. We suggest that feature D (Ekhe-Burkhan Corona feature) no longer be considered a corona. We also suggest that features A and B be considered within the same class, features A/B. We further recommend that features C be classified as a suite of features different from features A/B. Although features A/B and C are similar in size (75 to 360 km in diameter) and planform shape (quasi-circular), these groups differ in both structural characteristics and topographic signature. Features C lack radial fractures, which characterize features A/B, and features C form circular topographic basins, whereas features A/B form quasi-circular domes.

The questions remain: how might features A/B and C have evolved, or what processes might these features record? Radial

fractures and radial flows represent two elements that might form during the evolution of circular geomorphic features and might, as such, provide clues to evolutionary processes. However, these two suites of features might not be similarly preserved on Venus. For example, radial flow surfaces can degrade with time and become more radar dark, and thus more difficult to observe in SAR images (Arvidson and others, 1992). Therefore the apparent absence of radial flows cannot be taken as evidence that radial flows did not form during the evolution of a specific feature. In contrast, because radial fractures represent mechanical discontinuities that impart a rheological anisotropy to a surface, the radial fractures, once formed, are harder to destroy or hide. Younger flows could cover radial fractures, although near complete burial would be required. Once fractures form (even if later buried), they can be reactivated depending on their orientation relative to later stress fields. Given that radial fracture suites include a wide range of fracture orientations (360° in the case of a well-defined radial suite), at least some of the fractures are likely to be of an orientation that could be reactivated during younger deformation. In addition, radial fractures can extend well beyond the topographic limits of a domical structure and, therefore, if topography decays the radial suite, would still be preserved across a large area. Because of this, the absence of radial fractures likely indicates that radial fractures never formed, rather that radial fractures formed but were not preserved. Thus the presence of characteristic radial fractures for features A/B and the absence of radial fractures for features C provide important clues about the operative mechanisms responsible for the formation of the two different feature classes. Features A/B record a process or processes that include radial fracture formation, whereas the process(es) responsible for the formation of features C should not form radial fractures.

The presence, or absence, of radial structures might place important constraints on the process(es) responsible for the formation of circular features such as coronae and montes. Radial fractures provide clues about the local state of stress during feature formation, the possible presence of magma at depth at the time of formation (for example, Grosfils and Head, 1994; Grindrod and others, 2005) and, equally important, once formed, radial fractures would typically be preserved.

Dome versus basin morphology also provides clues for feature evolution. Domes can form as a result of subsurface rise (primary dome formation). Basins can form as a result of subsurface subsidence (primary basin formation) or early subsurface rise, followed by later subsidence (secondary basin formation).

Three factors taken together—planform shape, presence or absence of radial structures, and primary versus secondary basin formation—might provide important clues for feature formation. Primary versus secondary basin formation make different predictions about planform shape and presence or absence of radial structures, as well as the geologic history.

Consider the case of secondary circular basin formation. The formation of circular (planform) domes should be accompanied by the formation of radial fractures, as proposed for corona formation, assuming the operative stresses exceed the elastic limit of the surface material (for example, Withjack and Scheiner, 1982; Cyr and Melosh, 1993; Koch and Manga, 1996). Radial fractures extend past the topographic limit of a domical feature, typically extending as much as one radius or more into the surrounding region. Although the formation of radial fractures might be suppressed in the case of an anisotropic regional stress field, the resulting feature should be elliptical rather than circular in planform (Withjack and Scheiner, 1982). Therefore, if a circular basin forms as a secondary feature related to post-doming subsidence, then radial fractures should have formed during the doming event. Once formed, the radial fractures should be preserved even in case of later subsidence and circular basin formation. The region of subsidence will be significantly less than the region affected by fractures, and thus the fractures will be preserved, even with later basin fill. In the case of circular lows (features C), the circular shape of the basin would seem to record (and require) an isotropic, rather than anisotropic, regional stress field during feature formation. Therefore, if the circular lows (features C) represent secondary basins, evidence of early formed radial fractures should be preserved. Given that each of the circular lows within V–45 lack any evidence for radial structures, these arguments suggest that the circular basins that define features C are likely primary basins, rather than secondary basins related to domical collapse.

Geologic mapping of these 12 geomorphic features is consistent with the interpretation that each geomorphic class—A/B, C, and D—record different, unrelated genetic processes. We suggest the following possible processes. Features A/B represent the surface expression of endogenic buoyant diapirs (for example, Stofan and others, 1992, 1997; Koch and Manga, 1996), likely driven by compositional rather than thermal buoyancy based on the relatively small size of these features (Hansen, 2003). Feature D (Ekhe-Burkhan) might represent the surface expression of a large lava pond (for example, Hansen, 2006) and (or) the spatial intersection of different tectonomagmatic events. Features C are perhaps the most enigmatic features, and they could have formed as a result of (1) exogenic bolide impact on rheologically relatively weak crust or by (2) endogenic processes. These endogenic processes include basin formation due to a negatively buoyant crustal diapir or magmatic evacuation processes, such as caldera formation or subsurface magma evacuation. Each of the processes outlined for the formation of features C could occur in concert with solidification of huge lava ponds, consistent with, but not required by, the observation that the circular lows within V–45 all lie in close proximity to ribbon-tessera terrain.

A global survey of circular lows documents 53 such features across Venus, with about half of these features occurring within the Venus lowland (Shankar and Hansen, 2008). The results of that study, taken in concert with results herein, suggest that circular lows might deserve additional detailed study, individually and collectively.

Perhaps the most important result to emerge from geologic mapping of V–45 coronae and montes is to question whether all coronae on Venus form in a similar fashion, or by a singular mechanism, or if Venusian coronae might represent a number of geomorphically distinct features formed by a variety of geological processes. Other workers have raised similar questions. For example, some geologists have proposed that coronae marked by large interior depressions might represent caldera

(for example, Stofan and others, 1991; Squyres and others, 1992; DeLaughter and Jurdy, 1999). Other geologists have suggested (mostly, but not all, prior to the acquisition of Magellan data) that some, or all, coronae represent impact craters (for example, Barsukov and others, 1986; Basilevsky and others, 1987; Campbell and Burns, 1979; Grieve and Head, 1981; Head and Solomon, 1981; Masursky and others, 1980; Schaber and Boyce, 1977; Nikolayeva and others, 1986; Nikolayeva, 1993; Schultz, 1993).

We suggest that the term "corona" be (1) used in a strict descriptive sense, free of genetic implications (note that this requires agreement by the community with regard to a descriptive definition of coronae); (2) redefined to include only a specific unique descriptive subset of Venusian coronae; or (3) abandoned as a term all together.

## Summary

In summary, V–45 records a rich geologic history spanning from ancient events to contemporary events. Ribbon-tessera terrain is divisible into several distinct packages based on fabric character, orientation, and spatial distribution. Distinct tracts of ribbon-tessera terrain record a series of diachronous events during their respective formation, including horizontal displacement of relatively large tracts of earlier formed ribbon tessera, as the solidified scum of huge lava ponds. Ribbon-tessera terrain in V–45 is structurally similar to ribbon-tessera terrain preserved in crustal plateaus, yet it consistently lies within a lowland, rather than highland, position. All viable hypotheses for ribbon-tessera formation should address this observation. The emplacement of shield terrain across much of V–45 locally masked the underlying ribbon-tessera fabrics. The formation of circular lows, a sub-set of corona (geomorphically defined rather than genetically defined) may have occurred late in the evolution of ribbon-tessera terrain. Circular lows could variably represent bolide impact on partially solidified lava ponds, or subsurface displacement of lava. Domical radial coronae and montes might also reflect different processes, including subsurface magma displacement related to lava pond solidification or buoyant crustal or lithospheric diapirs unrelated to lava pond solidification. Circular lows, a distinctive class of coronae features marked by circular basins and concentric fractures zones, differ from many coronae, notably lacking radial fractures, long lava flows, and positive topography. Circular lows might represent a different class and origin than other coronae.

## References Cited


Addington, E.A., 2001, A stratigraphic study of small volcano clusters on Venus: Icarus, v. 149, p. 16–36.

Arvidson, R.E., Greeley, R., Malin, M.C., and 5 others, 1992, Surface modification of Venus as inferred from Magellan observation of plains: Journal of Geophysical Research, v. 97, p. 13303–13318.

Baker, V.R., Komatsu, G., Gulick, V.C., and Parker, T.J., 1997, Channels and valleys, *in* Bouger, S.W., Hunten, D.M., and Phillips, R.J., eds., Venus II: Tucson, University of Arizona Press, p. 757–798.

Baker, V.R., Komatsu, G., Parker, T.J., and 3 others, 1992, Channels and valleys on Venus—Preliminary analysis of Magellan data: Journal of Geophysical Research, v. 97, p. 13395–13420.

Banerdt, W.B., McGill, G.E., and Zuber, M.T., 1997, Plains tectonics on Venus, *in* Bouger, S.W., Hunten, D.M., and Phillips, R.J., eds., Venus II: University of Arizona Press, p. 901–930.

Banerdt, W.B., and Sammis, C.G., 1992, Small-scale fracture patterns on the volcanic plains of Venus: Journal of Geophysical Research, v. 97, p. 16149–16166.

Banks, B.K., and Hansen, V.L., 2000, Relative timing of crustal plateau magmatism and tectonism at Tellus Regio, Venus: Journal of Geophysical Research, v. 105, p. 17655–17668.

Bannister, R.A., and Hansen, V.L., 2010, Geologic map of the Artemis quadrangle (V–48), Venus: U.S. Geological Survey Scientific Investigations Map 3099, scale 1:5,000,000 [http://pubs.usgs.gov/sim/3099/].

Barsukov, V.L., Basilevsky, A.T., Burba, G.A., and 27 others, 1986, The geology and geomorphology of the Venus surface as revealed by the radar images obtained by Veneras 15 and 16: Journal of Geophysical Research, v. 91, p. D378–D398.

Basilevsky, A.T., and Head, J.W., 1995, Regional and global stratigraphy of Venus—A preliminary assessment and implications for the geological history of Venus: Planetary Space Science, v. 43, p. 1523–1553.

Basilevsky, A.T., and Head, J.W., 2002, Venus—Analysis of the degree of impact crater deposit degradation and assessment of its use for dating geological units and features: Journal of Geophysical Research–Planets, v. 107, no. E8, doi: 10.1029/2001JE001584.

Basilevsky, A.T., Head, J.W., Schaber, G.G., and Strom, R.G., 1997, The resurfacing history of Venus, *in* Bouger, S.W., Hunten, D.M., and Phillips, R.J., eds., Venus II: Tucson, University of Arizona Press, p. 1047–1086.

Basilevsky, A.T., Ivanov, B.A., Burba, G.A., and 5 others, 1987, A continuation of the analysis of data from the Venera 15 and 16 spacecraft: Journal of Geophysical Research, v. 92, no. 12, p. 12869–12912.

Berthé, D., Choukroune, P., and Jegouzo, P., 1979, Orthogneiss, mylonite and noncoaxial deformation of granite—The example of the South Armoricain shear zone: Journal of Structural Geology, v. 1, p. 31–42.

Bindschadler, D.L., deCharon, A., Beratan, K.K., and Head, J.W., 1992, Magellan observations of Alpha Regio—Implications for formation of complex ridged terrains on Venus: Journal of Geophysical Research, v. 97, p. 13563–13577.

Bleamaster, L.F., III, and Hansen, V.L., 2005, Effects of crustal heterogeneity on the morphology of chasmata, Venus: Journal of Geophysical Research, v. 109, no. E2, 10.1029/2003JE002193.

Bridges, N.T., and McGill, G.E., 2002, Geologic map of the Kaiwan Fluctus quadrangle (V–44), Venus: U.S. Geological Survey Geologic Investigations Series I–2747, scale 1:5,000,000 [http://pubs.usgs.gov/i-map/i2747/].

Brown, C.D., and Grimm, R.E., 1999, Recent tectonic and lithospheric thermal evolution of Venus: Icarus, v. 139, no. 1, p. 40–48.
Campbell, B.A., 1999, Surface formation rates and impact crater densities on Venus: Journal of Geophysical Research, v. 104, no. E9, p. 21,951–21,955.
Campbell, D. B., and Burns, B. A., 1979, Venus—Further evidence of impact cratering and tectonic activity from radar observations: Science, v. 204, p. 1424–1427.
Crumpler, L.S., Aubele, J.C., Senske, D.A., and 3 others, 1997, Volcanoes and centers of volcanism on Venus, *in* Bouger, S.W., Hunten, D.M., and Phillips, R.J., eds., Venus II—Geology, geophysics, atmosphere, and solar wind environment: Tucson, University of Arizona Press, p. 697–756.
Cyr, K.E., and Melosh, H.J., 1993, Tectonic patterns and regional stresses near Venusian coronae: Icarus, v. 102, p. 175–184.
DeLaughter, J.E., and Jurdy, D.M., 1999, Corona classification by evolutionary stage: Icarus, v. 139, no. 1, p. 81.
Deshon, H.R., Young, D.A., and Hansen, V.L., 2000, Geologic evolution of southern Rusalka Planitia, Venus: Journal of Geophysical Research, v. 105, p. 6983–6995.
Ferrill, D.A., Wyrick, D.Y., Morris, A.P., Sims, D.W., and Franklin, N.M., 2004, Dilational fault slip and pit chain formation on Mars: GSA Today, v. 14, no. 10, p. 1–9.
Ford, J.P., Plaut, J.J., Weitz, C.M., and 5 others, 1993, Guide to Magellan image interpretation: National Aeronautics and Space Administration Jet Propulsion Laboratory Publication, 148 p.
Ghail, R.C., 2002, Structure and evolution of southeast Thetis Regio: Journal of Geophysical Research, v. 107, no. E8, p. 5060.
Ghent, R.R., and Hansen, V.L., 1999, Structural and kinematic analysis of eastern Ovda Regio, Venus—Implications for crustal plateau formation: Icarus, v. 139, p. 116–136.
Ghent, R.R., and Tibuleac, I.M., 2002, Ribbon spacing in Venusian tessera—Implications for layer thickness and thermal state: Geophysical Research Letters, v. 29, no. 20, p. 994–997.
Gilbert, G.K., 1886, Inculcation of the scientific method: American Journal of Science, v. 31, p. 284–299.
Gilmore, M.S., Collins, G.C., Ivanov, M.A., Marinangeli, L., and Head, J.W., 1998, Style and sequence of extensional structures in tessera terrain, Venus: Journal of Geophysical Research, v. 103, no. E7, p. 16813–16840.
Grieve, R.A.F., and Head, J.W., 1981, Impact cratering, a geological process on the planets: Episodes, v. 4, no. 2, p. 3–9.
Grindrod, P.M., Nimmo, F., Stofan, E.R., and Guest, J.E., 2005, Strain at radially fractured centers on Venus: Journal of Geophysical Research, v. 110, no. E12002, doi:10.1029/2005JE002416.
Grosfils, E.B., and Head, J.W., 1994, Emplacement of a radiating dike swarm in western Vinmara Planitia, Venus—Interpretation of the regional stress-field orientation and subsurface magmatic configuration: Earth, Moon, and Planets, v. 66, no. 2, p. 153–171.
Guest, J.E., Bulmer, M.H., Aubele, J.C., and 6 others, 1992, Small volcanic edifices and volcanism in the plains on Venus: Journal of Geophysical Research, v. 97, p. 15949–15966.
Guest, J.E., and Stofan, E.R., 1999, A new view of the stratigraphic history of Venus: Icarus, v. 139, p. 55–66.
Hamilton, W.B., 2005, Plumeless Venus has ancient impact-accretionary surface, *in* Foulger, G.R., Natland, J.H., Presnall, D.C., and Anderson, D.L., eds., Plates, plumes, and paradigms: Geological Society of America Special Paper, p. 781–814.
Hansen, V.L., 1992, Regional non-coaxial deformation on Venus—Evidence from western Izpapalotl Tessera: Lunar and Planetary Science XXIII, p. 478–479.
Hansen, V.L., 2000, Geologic mapping of tectonic planets: Earth and Planetary Science Letters, v. 176, p. 527–542.
Hansen, V.L., 2002, Artemis—Signature of a deep Venusian mantle plume: Geological Society of America Bulletin, v. 114, no. 7, p. 839–848.
Hansen, V.L., 2003, Venus diapirs—Thermal or compositional?: Geological Society of America Bulletin, v. 115, no. 9, p. 1040–1052.
Hansen, V.L., 2005, Venus's shield-terrain: Geological Society of America Bulletin, v. 117, no. 5/6, p. 808–822.
Hansen, V.L., 2006, Geologic constraints on crustal plateau surface histories, Venus—The lava pond and bolide impact hypotheses: Journal of Geophysical Research, v. 111, no. E11010, doi:10.1029/2006JE002714.
Hansen, V.L., 2008, Geologic map of the Niobe Planitia quadrangle (V–23), Venus: U.S. Geological Survey Scientific Investigations Map 3025, scale 1:5,000,000 [http://pubs.usgs.gov/sim/3025/].
Hansen, V.L., Banks, B.K., and Ghent, R.R., 1999, Tessera terrain and crustal plateaus, Venus: Geology, v. 27, p. 1071–1074.
Hansen, V.L., and Lopez, I., 2010, Venus records a rich early history: Geology, v. 38, no. 4, p. 311–314, doi:10.1130/G30587.1.
Hansen, V.L., and Olive, A., 2010, Artemis, Venus—The largest tectonomagmatic feature in the solar system?: Geology, v. 38, no. 5, p. 467–470; doi:10.1130/G30643.1.
Hansen, V.L., Phillips, R.J., Willis, J.J., and Ghent, R.R., 2000, Structures in tessera terrain, Venus—Issues and answers: Journal of Geophysical Research, v. 105, p. 4135–4152.
Hansen, V.L., and Willis, J.J., 1996, Structural analysis of a sampling of tesserae—Implications for Venus geodynamics: Icarus, v. 123, no. 2, p. 296–312.
Hansen, V.L., and Willis, J.J., 1998, Ribbon terrain formation, southwestern Fortuna Tessera, Venus—Implications for lithosphere evolution: Icarus, v. 132, p. 321–343.
Hansen, V.L., Willis, J.J., and Banerdt, W.B., 1997, Tectonic overview and synthesis, *in* Bouger, S.W., Hunten, D.M., and Phillips, R.J., eds., Venus II: University of Arizona Press, p. 797–844.

Hansen, V.L., and Young, D.A., 2007, Venus's evolution—A synthesis, *in* Cloos, M., Carlson, W.D., Gilbert, M.C., Liou, J.G., and Sorensen, S.S., eds., Convergent margin terranes and 6 associated regions—A Tribute to W.G. Ernst: Geological Society of America, p. 255–273, 10.1130/2006.2419(13).

Hauck, S.A., Phillips, R.J., and Price, M.H., 1998, Venus—Crater distribution and plains resurfacing models: Journal of Geophysical Research, v. 103, no. 6, p. 13635–13642.

Head, J.W., and Solomon, S.C., 1981, Tectonic evolution of the terrestrial planets: Science, v. 213, p. 62–76.

Herrick, R.R., 1994, Resurfacing history of Venus: Geology, v. 22, p. 703–706.

Herrick, R.R., 2006, Updates regarding the resurfacing of Venusian impact craters: Lunar and Planetary Science Conference XXXVII, Houston, Tex., abstract 1588 [CD ROM].

Herrick, R.R., and Rumpf, M.E., 2011, Post-impact modification by volcanic or tectonic processes as the rule, not the exception, for Venusian craters: Journal of Geophysical Research–Planets, v. 116, no. E02004, doi:10.1029/2010JE003722.

Herrick, R.R., and Sharpton, V.L., 2000, Implications from stereo-derived topography of Venusian impact craters: Journal of Geophysical Research–Planets, v. 105, no. E8, p. 20245–20262.

Herrick, R.R., Sharpton, V.L., Malin, M.C., Lyons, S.N., and Feely, K., 1997, Morphology and morphometry of impact craters, *in* Bouger, S.W., Hunten, D.M., and Phillips, R.J., eds., Venus II: Tucson, University of Arizona Press, p. 1015–1046.

Ignacio, R., Ramo´n, C., and Francisco, A., 2005, Tectonic and kinematic study of a strike-slip zone along the southern margin of central Ovda Regio, Venus—Geodynamical implications for crustal plateaux formation and evolution: Icarus, v. 175, p. 320–334.

Ivanov, M.A., and Head, J.W., 1996, Tessera terrain on Venus—A survey of the global distribution, characteristics, and relation to surrounding units from Magellan data: Journal of Geophysical Research, v. 101, no. 6, p. 14861–14908.

Izenberg, N.R., Arvidson, R.E., and Phillips, R.J., 1994, Impact crater degradation on Venusian plains: Geophysical Research Letters, v. 21, p. 289–292.

Kirk, R., Soderblom, L., and Lee, E., 1992, Enhanced visualization for interpretation of Magellan radar data—Supplement to the Magellan special issue: Journal of Geophysical Research, v. 97, p. 16371–16380.

Koch, D.M., and Manga, M., 1996, Neutrally buoyant diapirs—A model for Venus coronae: Geophysical Research Letters, v. 23, p. 225–228.

Kumar, P.S., 2005, An alternative kinematic interpretation of Thetis Boundary Shear Zone, Venus: Journal of Geophysical Research, v. 110, no. E07001.

Lang, N.P., and Hansen, V.L., 2008, Geologic map of the Greenaway quadrangle (V–24), Venus: U.S. Geological Survey Scientific Investigations Map 3089, scale 1:5,000,000 [http://pubs.usgs.gov/sim/3089].

Mackwell, S.J., Zimmerman, M.E., and Kohlstedt, D.L., 1998, High-temperature deformation of dry diabase with application to tectonics on Venus: Journal of Geophysical Research, v. 102, p. 975–984.

Masursky, H., Eliason, E., Ford, P.G., and 4 others, 1980, Pioneer Venus radar results—Geology from images and altimetry: Journal of Geophysical Research, v. 85, p. 8232–8260.

McDaniel, K., and Hansen, V.L., 2005, Circular lows, a genetically distinct subset of coronae?: Lunar and Planetary Science Conference XXXVI, Houston, Tex., abstract 2367 [CD ROM].

McGill, G.E., 2004, Tectonic and stratigraphic implications of the relative ages of Venusian plains and wrinkle ridges: Icarus, v. 172, no. 2, p. 603–612.

McGill, G.E., and Campbell, B.A., 2004, Ages of Venusian ridge belts relative to regional plains: Lunar and Planetary Science Conference XXXVI, Houston, Tex., abstract 1143 [CD ROM].

McKinnon, W.B., Zahnle, K.J., Ivanov, B.A., and Melosh, H.J., 1997, Cratering on Venus—Models and observations, *in* Bouger, S.W., Hunten, D.M., and Phillips, R.J., eds., Venus II: Tucson, University of Arizona Press, p. 969–1014.

Nikolayeva, O.V., 1993, Largest impact features on Venus—Non-preserved or non-recognizable?: Lunar and Planetary Science Conference XXIV, Houston, Tex., p. 1083–1084 [abstract].

Nikolayeva, O.V., Ronca, L.B., and Bazilevskiy, A.T., 1986, Circular structures on the plains of Venus as evidence of its geologic history: Geokhimiya, v. 5, p. 579–589.

Okubo, C.H., and Martel, S.J., 1998, Pit crater formation on Kilauea volcano, Hawaii: Journal of Volcanology and Geothermal Research, v. 86, no. 14, p. 1–8.

Parmentier, E.M., and Hess, P.C., 1992, Chemical differentiation of a convecting planetary interior—Consequences for a one plate planet such as Venus: Geophysical Research Letters, v. 19, p. 2015–2018.

Phillips, R.J., 1993, The age spectrum of the Venusian surface: Eos (Supplement), v. 74, no. 16, p. 187.

Phillips, R.J., and Hansen, V.L., 1994, Tectonic and magmatic evolution of Venus: Annual Reviews of the Earth and Planetary Sciences, v. 22, p. 597–654.

Phillips, R.J., and Hansen, V.L., 1998, Geological evolution of Venus—Rises, plains, plumes and plateaus: Science, v. 279, p. 1492–1497.

Phillips, R.J., and Izenberg, N.R., 1995, Ejecta correlations with spatial crater density and Venus resurfacing history: Geophysical Research Letters, v. 22, no. 12, p. 1517–1520.

Phillips, R.J., Raubertas, R.F., Arvidson, R.E., and 4 others, 1992, Impact crater distribution and the resurfacing history of Venus: Journal of Geophysical Research, v. 97, p. 15923–15948.

Romeo, I., Capote, R., and Anguita, F., 2005, Tectonic and kinematic study of a strike-slip zone along the southern margin of Central Ovda Regio, Venus—Geodynamical implications for crustal plateaux formation and evolution: Icarus, v. 175, p. 320–334.

Ruiz, J., 2007, The heat flow during formation of ribbon terrains on Venus: Planetary and Space Science, v. 55, p. 2063–2070, doi:10.1016/j.icarus.204.11.007.
Schaber, G.G., and Boyce, J.M., 1977, Probable distribution of large impact basins on Venus—Comparison with Mercury and the Moon, *in* Roddy, D.J., Pepin, R.O., and Merrill, R.B., eds., Impact and explosion cratering—Planetary and terrestrial implications: New York, Pergamon Press, p. 603–612.
Schaber, G.G., Strom, R.G., Moore, H.J., and 7 others, 1992, Geology and distribution of impact craters on Venus—What are they telling us?: Journal of Geophysical Research, v. 97, p. 13257–13302.
Schultz, P.H., 1993, Searching for ancient Venus: Lunar and Planetary Science Conference XXIV, Houston, Tex., 1255–1256.
Schultz, R.A., Okubo, C.H., Goudy, C.L., and Wilkins, S.J., 2004, Igneous dikes on Mars revealed by Mars Orbiter Laser Altimeter topography: Geology, v. 32, p. 889–892.
Shankar, B., and Hansen, V.L., 2008, Preliminary global survey of circular lows—A subset of Venusian coronae: Lunar and Planetary Science Conference XXXIX, Houston, Tex., abstract 1813 [PDF].
Skinner, J.A., and Tanaka, K.L., 2003, How should map units be defined?: Lunar and Planetary Science Conference XXXIV, Houston, Tex., abstract 2100 [PDF].
Solomon, S.C., 1993, The geophysics of Venus: Physics Today, v. 46, no. 7, p. 48–55.
Squyres, S.W., Janes, D.M., Baer, G., and 4 others, 1992, The morphology and evolution of coronae on Venus: Journal of Geophysical Research, v. 97, p. 13611–13634.
Steinbach, V., and Yuen, D.A., 1992, The effects of multiple phase transitions on Venusian mantle convection: Geophysical Research Letters, v. 19, no. 22, p. 2243–2246.
Stofan, E.R., Bindschadler, D.L., Head, J.W., and Parmentier, E.M., 1991, Corona structures on Venus—Models of origin: Journal of Geophysical Research, v. 96, p. 20933–20946.
Stofan, E.R., Brian, A.W., and Guest, J.E., 2005, Resurfacing styles and rates on Venus—Assessment of 18 Venusian quadrangles: Icarus, v. 173, p. 312–321.
Stofan, E.R., and Guest, J.E., 2003, Geologic map of the Aino Planitia quadrangle (V–46), Venus: U.S. Geological Survey Geologic Investigations Series I–2779, scale 1:5,000,000 [http://pubs.usgs.gov/i-map/i2779/].
Stofan, E.R., Hamilton, V.E., Janes, D.M., and Smrekar, S.E., 1997, Coronae on Venus—Morphology and origin, *in* Bouger, S.W., Hunten, D.M., and Phillips, R.J., eds., Venus II: Tucson, University of Arizona Press, p. 931–968.
Stofan, E.R., Senske, D.A., and Michaels, G., 1993, Tectonic features in Magellan data, *in* Ford, P.J., Plaut, J., Wietz, C.M., and 5 others, eds., Guide to Magellan image interpretation: Pasadena, Calif., National Aeronautics and Space Administration Jet Propulsion Laboratory, p. 93–108.
Stofan, E.R., Sharpton, V.L., Schubert, G., and 4 others, 1992, Global distribution and characteristics of coronae and related features on Venus—Implications for origin and relation to mantle processes: Journal of Geophysical Research, v. 97, p. 13347–13378.
Stofan, E.R., Tapper, S., Guest, J.E., and Smrekar, S.E., 2001, Preliminary analysis of an expanded database of coronae on Venus: Geophysical Research Letters, v. 28, p. 4267–4270.
Strom, R.G., Schaber, G.G., and Dawson, D.D., 1994, The global resurfacing of Venus: Journal of Geophysical Research, v. 99, p. 10899–10926.
Tanaka, K.L., comp., 1994, The Venus geologic mappers' handbook (2nd ed.): U.S. Geological Survey Open-File Report 94–438, 68 p.
Tuckwell, G.W., and Ghail, R.C., 2003, A 400-km-scale strike-slip zone near the boundary of Thetis Regio, Venus: Earth and Planetary Science Letters, v. 211, no. 1–2, p. 45–55.
Turcotte, D.L., 1993, An episodic hypothesis for Venusian tectonics: Journal of Geophysical Research, v. 98, no. E9, p. 17061–17068.
Turcotte, D.L., Morein, G., and Malamud, B.D., 1999, Catastrophic resurfacing and episodic subduction on Venus: Icarus, v. 139, no. 1, p. 49–54.
Vita-Finzi, C., Howarth, R.J., Tapper, S.W., and Robinson, C.A., 2005, Venusian craters, size distribution and the origin of coronae, *in* Foulger, G.R., Natland, J.H., Presnall, D.C., and Anderson, D.L., eds., Plates, plumes, and paradigms: Denver, Geological Society of America, p. 815–824.
Watters, T.R., 1988, Wrinkle ridge assemblages on the terrestrial planets: Journal of Geophysical Research, v. 93, no. 10, p. 236–254.
Wilhelms, D.E., 1990, Geologic mapping, *in* Greeley, R., and Batson, R.M., eds., Planetary mapping: New York, Cambridge University Press, p. 208–260.
Withjack, M.O., and Scheiner, C., 1982, Fault patterns associated with domes—An experimental and analytical study: American Association of Petroleum Geologists Bulletin, v. 66, no. 3, p. 302–316.
Zimbelman, J.R., 2001, Image resolution and evaluation of genetic hypotheses for planetary landscapes: Geomorphology, v. 37, no. 3–4, p. 179–199.

**Table 1.** Impact craters of Agnesi quadrangle (V–45), Venus.

[Y, yes; N, no; P, possible; I, indeterminate due to large variation in local radar backscatter or data resolution]

| Crater name | Center latitude (deg. S.) | Center longitude (deg. E.) | Diameter (km) | Crater density[1] | Unit where located | Ejecta blanket | Impact halo | Central peak | Rim | Interior flood deposits | Elevation (km) |
|---|---|---|---|---|---|---|---|---|---|---|---|
| Agnesi | 39.5 | 37.7 | 41.40 | 2.86479 | rtE, fu[2] | Y | I | Y | Y | Y | 6051.76 |
| Anicia | 26.3 | 31.3 | 38.40 | 1.59155 | rtc, s[2] | Y | N | Y | Y | Y | 6051.89 |
| Francesca | 28.0 | 57.7 | 17.10 | 2.86479 | fsu | Y | Y | Y? | Y | N | 6051.28 |
| Kalombo | 30.5 | 34.0 | 9.40 | 1.59155 | $rtP_b$, rtc[2], s[2] | Y | N | N | Y | P | 6051.97 |
| Kastush | 28.6 | 60.0 | 12.70 | 2.54648 | fsu | Y | Y | Y? | Y | N | 6051.23 |
| Kimitonga | 25.0 | 48.3 | 4.70 | 2.22817 | fsu | Y | Y | N | Y | N | 6051.83 |
| Kosi | 43.9 | 55.0 | 7.20 | 0.95493 | fCGM | Y | Y | N | Y | N | 6051.3 |
| Lehmann | 44.1 | 39.1 | 22.80 | 1.27324 | fUA[2] | Y | I | Y | Y | Y | 6051.5 |
| Lockwood | 32.9 | 51.6 | 22.20 | 2.22817 | $rtP_c$, dZa[2] | Y | N | Y | Y | Y | 6051.88 |
| Masako | 30.2 | 53.2 | 23.80 | 2.54648 | s[2], fsu[2] | Y | I | Y | Y | Y | 6051.68 |
| Nomeda | 49.2 | 55.5 | 12.00 | 1.59155 | fCGM | Y | Y | Y | Y | N | 6051.87 |
| Purev | 31.1 | 46.5 | 11.60 | 1.27324 | fsu[2] | Y | N | N | Y | Y | 6052.1 |
| Yoshioka | 32.4 | 58.9 | 16.70 | 2.86479 | rtTX | Y | N | N | Y | Y | 6051.46 |

[1]Crater density (values from Herrick and others, 1997) at a crater's location (Rho). Value is the density of craters in the neighborhood of a specified crater. This was calculated by counting the number of craters (including the specified crater) within a 1,000-km-radius circle and normalizing to give the number of craters per 1 x $10^6$ $km^2$.

[2]Indicates units adjacent to crater ejecta, but units are not necessarily older than crater ejecta (see text for discussion).

**Table 2.** Characteristics of coronae, corona-like features, and montes within Agnesi quadrangle (V–45), Venus.

[dep, deposit; fo, folds; fr, fractures; n, none; N, no; ND, not determined; P, possible; post, post-dates rtt units; rtt, ribbon tessera terrain; Str, structures; syn, synchronous with rtt units; Y, yes]

| Feature name | Latitude/longitude | Diameter (km) | Ellipticity | Topographic form | Concentric | | Radial | | Flows/deposit | | rtt | Feature[1] |
|---|---|---|---|---|---|---|---|---|---|---|---|---|
| | | | | | Ridge? | Str | Str | Flows | Internal | Shields | | |
| Codidon Corona | 46° S./56° E. | 250 | ~0.65 | dome | Y | fr | Y | Y | NA | Y | ND | A |
| Ekhebukman Corona[2] | 50° S./40° E. | 600[1] | NA | varied | P | fo | P | P | Y | Y | syn | D |
| Elihino Corona[3] | 37° S./49° E. | 200 | ~0.75 | dome | N | fr | N | N | Y | Y | post | C |
| Gurshi Mons | 47.5° S./58.5° E. | 210 | >0.85 | dome | N | n | Y | Y | NA | Y | ND | B |
| Inanna Corona | 37° S./35.9° E. | 350 | <0.75 | dome | Y | fr | Y | Y | NA | Y | post | A |
| MamaAllpa Corona | 27° S./31° E. | 300 | ~1 | basin | Y | fr | N | N | Y | Y | post | C |
| Mounyamy Corona | 49.5° S./59° E. | 200 | <0.75 | dome | N | n | Y | P | NA | Y | ND | A |
| Pakoti Corona[3] | 38° S./42.5° E. | 75 | ~1 | basin | N | fr | N | N | Y | Y | post | C |
| Tuzandi Mons | 42.5° S./41.5° E. | 200 | >0.85 | dome | N | n | Y | P | NA | Y | post | B |
| Umay-ene Corona | 27.5° S./50.5° E. | 370 | >0.85 | basin | P | fr | N | N | Y | Y | post | C |
| Xcanil Corona | 37° S./43° E. | 150 | ~1 | basin | N | fr | N | N | Y | Y | post | C |
| Zemlika Corona | 33.5° S./50° E. | 150 | ~1 | basin | Y | fr | N | dep | Y | Y | post | C |

[1]Coronae and montes geomorphic group: A, domical structures with ellipicity <0.75, radial features, and variably developed (or preserved) radial flows; B, similar to A except more circular in planform and lacking concentric structures; C, basinal structures with nearly circular planform (ellipticity >0.85), decorated with concentric structures and lacking evidence for radial structures and (or) radial flows; D, differs from other features with plateau-like form, structural fabric akin to ribbon-tessera terrain, and lack of well-defined circular boundaries or limits.

[2]See discussion in text (no longer considered corona or mons).

[3]Corona-like feature.